BAMS Article

The Innovative Strategies for Observations in the Arctic Atmospheric Boundary Layer Project (ISOBAR)

Unique Finescale Observations under Stable and Very Stable Conditions

Stephan T. Kral, Joachim Reuder, Timo Vihma, Irene Suomi, Kristine F. Haualand, Gabin H. Urbancic, Brian R. Greene, Gert-Jan Steeneveld, Torge Lorenz, Björn Maronga, Marius O. Jonassen, Hada Ajosenpää, Line Båserud, Phillip B. Chilson, Albert A. M. Holtslag, Alastair D. Jenkins, Rostislav Kouznetsov, Stephanie Mayer, Elizabeth A. Pillar-Little, Alexander Rautenberg, Johannes Schwenkel, Andrew W. Seidl, and Burkhard Wrenger

ABSTRACT: The Innovative Strategies for Observations in the Arctic Atmospheric Boundary Layer Program (ISOBAR) is a research project investigating stable atmospheric boundary layer (SBL) processes, whose representation still poses significant challenges in state-of-the-art numerical weather prediction (NWP) models. In ISOBAR ground-based flux and profile observations are combined with boundary layer remote sensing methods and the extensive usage of different unmanned aircraft systems (UAS). During February 2017 and 2018 we carried out two major field campaigns over the sea ice of the northern Baltic Sea, close to the Finnish island of Hailuoto at 65°N. In total 14 intensive observational periods (IOPs) resulted in extensive SBL datasets with unprecedented spatiotemporal resolution, which will form the basis for various numerical modeling experiments. First results from the campaigns indicate numerous very stable boundary layer (VSBL) cases, characterized by strong stratification, weak winds, and clear skies, and give detailed insight in the temporal evolution and vertical structure of the entire SBL. The SBL is subject to rapid changes in its vertical structure, responding to a variety of different processes. In particular, we study cases involving a shear instability associated with a low-level jet, a rapid strong cooling event observed a few meters above ground, and a strong wave-breaking event that triggers intensive near-surface turbulence. Furthermore, we use observations from one IOP to validate three different atmospheric models. The unique finescale observations resulting from the ISOBAR observational approach will aid future research activities, focusing on a better understanding of the SBL and its implementation in numerical models.

KEYWORDS: Atmosphere; Arctic; Boundary layer; Numerical analysis/modeling; Field experiments

https://doi.org/10.1175/BAMS-D-19-0212.1
Corresponding author: Stephan T. Kral, stephan.kral@uib.no
In final form 9 September 2020

AFFILIATIONS: Kral, Reuder, Haualand, and Seidl—Geophysical Institute, and Bjerknes Centre for Climate Research, University of Bergen, Bergen, Norway; **Vihma, Suomi, and Ajosenpää**—Finnish Meteorological Institute, Helsinki, Finland; **Urbancic**—Geophysical Institute, University of Bergen, Bergen, Norway, and Finnish Meteorological Institute, Helsinki, Finland; **Greene and Chilson**—Advanced Radar Research Center, School of Meteorology, and Center for Autonomous Sensing and Sampling, University of Oklahoma, Norman, Oklahoma; **Steeneveld and Holtslag**—Meteorology and Air Quality Section, Wageningen University, Wageningen, Netherlands; **Lorenz and Mayer**—Norwegian Research Centre (NORCE), and Bjerknes Centre for Climate Research, Bergen, Norway; **Maronga**—Institute of Meteorology and Climatology, Leibniz University Hannover, Hannover, Germany, and Geophysical Institute, University of Bergen, Bergen, Norway; **Jonassen**—The University Centre in Svalbard, Longyearbyen, Norway, and Geophysical Institute, University of Bergen, Bergen, Norway; **Båserud**—Geophysical Institute, and Bjerknes Centre for Climate Research, University of Bergen, Bergen, and Norwegian Meteorological Institute, Oslo, Norway; **Jenkins**—Geophysical Institute, University of Bergen, Bergen, Norway; **Kouznetsov**—Finnish Meteorological Institute, Helsinki, Finland, and Obukhov Institute for Atmospheric Physics, Moscow, Russia; **Pillar-Little**—School of Meteorology, and Center for Autonomous Sensing and Sampling, University of Oklahoma, Norman, Oklahoma; **Rautenberg**—Center for Applied Geoscience, Eberhard-Karls-Universität Tübingen, Tübingen, Germany; **Schwenkel**—Institute of Meteorology and Climatology, Leibniz University Hannover, Hannover, Germany; **Wrenger**—Ostwestfalen-Lippe University of Applied Sciences and Arts, Höxter, Germany

The stably stratified atmospheric boundary layer (SBL; see Table A1 in the appendix for a list of abbreviations and expansions) is common in the Arctic, where the absence of solar radiation during winter causes a negative net radiation at the surface. Even during daylight seasons, the high surface albedo of snow and ice favors SBL formation (Persson et al. 2002). The SBL is of particular interest for our understanding of the Arctic climate system (e.g., Bintanja et al. 2012; Lesins et al. 2012; Davy and Esau 2016), which experiences a significantly stronger warming than the rest of the globe, commonly referred to as Arctic amplification (Serreze et al. 2009; Serreze and Barry 2011; Pithan and Mauritsen 2014; Dai et al. 2019). The state of and the processes in the ABL affect the turbulent and radiative heat fluxes from the atmosphere to Earth's surface and, accordingly, the surface mass balance of sea ice, ice sheets, glaciers, and terrestrial snow. Hence, the correct understanding and parameterization of the SBL and its coupling to the underlying snow, ice, or land surface is crucial for the reliability of climate model projections in polar regions. Another strong indication for the importance of the SBL is the fact that the observed global warming trend over the last decades is most pronounced at nighttime and in polar regions, both when SBLs prevail (McNider et al. 2010).

Climate and numerical weather prediction (NWP) models suffer from insufficient atmospheric boundary layer (ABL) parameterizations and have a strong need for an improved representation of the SBL, in particular in very stable boundary layer (VSBL) conditions. This is demonstrated by large errors under VSBL conditions, where 2-m air temperature errors ($\Delta T_{2\mathrm{m}}$) on the order of 10 K are common even in short-term (24-h) NWP products (Atlaskin and Vihma 2012). In atmospheric reanalyses, broadly applied in diagnostics of climate variability and change, the monthly/seasonal means of $\Delta T_{2\mathrm{m}}$ in the Arctic (Jakobson et al. 2012; Graham et al. 2019) and Antarctic (Jonassen et al. 2019) typically show values of a few kelvins, and can even reach 20 K, strongly depending on the VSBL parameterization applied (Uppala et al. 2005). The common positive temperature biases are typically related to excessively large downward sensible heat flux (Cuxart et al. 2005; Tjernström et al. 2005), whereas large negative biases may be generated via thermal decoupling between the atmosphere and the snow/ice surface (Mahrt 2003; Uppala et al. 2005). In addition to problems in the turbulence parameterization, most climate models use a too coarse vertical resolution for an appropriate representation of the VSBL (Byrkjedal et al. 2007).

The numerical models used for weather prediction and climate scenarios rely on turbulence closure and surface-layer exchange schemes based on Monin–Obukhov similarity theory (MOST; Monin and Obukhov 1954), which relates the nondimensional vertical gradients of wind, temperature, and humidity to their respective surface fluxes. MOST is, however, theoretically only valid for stationary, homogeneous flow fields in the atmospheric surface layer, where variations of the turbulent fluxes with height can be neglected. Because the SBL rarely satisfies these conditions, there is substantial need for improvement in the description, characterization, and parameterization of the relevant SBL processes. Moreover, empirical studies evaluating MOST commonly indicate an inability to differentiate between near-neutral and very stable regimes (Foken 2006; Sorbjan and Grachev 2010; Sorbjan 2010; Grachev et al. 2013), which is largely related to the very weak turbulent heat fluxes present in both situations.

The motivation of the Innovative Strategies for Observations in the Arctic Atmospheric Boundary Layer (ISOBAR) project is to improve our understanding of the SBL by applying new observation techniques and numerical modeling experiments, based on the collected data (see the sidebar "SBL model simulations" for an illustration of current SBL issues based on three different types of numerical models). In combination with well-established ground-based micrometeorological instrumentation and boundary layer remote sensing, we utilize multiple unmanned aircraft systems (UAS)—designed for boundary layer observations—to intensively sample the SBL over sea ice. Through this endeavor, we aim to advance our understanding of the myriad of different processes relevant under very stable stratification. The potential of such observational approaches has been emphasized in a number of SBL review articles (e.g., Fernando and Weil 2010; Mahrt 2014). In particular, we investigate the role of wave–turbulence interaction, the formation and variability of low-level jets (LLJ), intermittency, the spatiotemporal evolution of the SBL structure, and interaction between the SBL and the free atmosphere.

The ABL is in general characterized by turbulence generated by wind shear that is either enhanced or suppressed by buoyancy effects, with surface friction and surface heating or cooling as the main drivers. SBL formation is favored by clear sky and weak wind conditions, typically associated with high pressure synoptic situations characterized by large-scale subsidence and weak pressure gradients. Warm air advection may also contribute to the formation or strengthening of an SBL. In SBL research, it is common to distinguish between the weakly stable boundary layer (WSBL), where turbulence is still the dominating process, and the VSBL, in which turbulence is weak or intermittent. Transitions between WSBL and VSBL take place under clear skies when the net radiative heat loss at the surface becomes larger than the maximum turbulent heat flux that can be maintained by wind shear (Van de Wiel et al. 2017). As turbulence in the VSBL is typically weak, other processes—such as radiation divergence, surface coupling, wave phenomena, and fog—may become more important. If present, the turbulence is often intermittent.

Hoch et al. (2007), Steeneveld et al. (2010), and Gentine et al. (2018) address the substantial role of radiation divergence on the temperature budget under these conditions. Moreover, the lack of turbulent drag in the VSBL coincides with the emergence of LLJ. Bosveld et al. (2014) showed that even for a relatively straightforward LLJ event at Cabauw (The Netherlands), different single-column models (SCM) represent this event rather differently and with considerable biases compared to observations. In addition, gravity waves might propagate under stratified conditions and transport momentum vertically (Nappo 2012; Lapworth and Osborne 2019). The sheer number of involved processes, and their often local nature, results in a rather poor understanding of the SBL in general (Mahrt 2014). An improved understanding of the SBL archetypes and their evolution is in particular hampered by the lack of available vertical profile observations of temperature, humidity and wind speed at an appropriate vertical resolution and at high enough sampling rates, as these variables may vary strongly in time and space.

In the WSBL, turbulence can be properly scaled following the local scaling hypothesis proposed by Nieuwstadt (1984), an extension of the original MOST. For the VSBL, classical scaling relations break down and a comprehensive theory is virtually absent. Previous studies successfully applied gradient-based scaling as a function of the gradient Richardson number, Ri (Sorbjan and Grachev 2010; Sorbjan 2010). This method is formally equivalent to MOST, but does not suffer from poorly defined scaling parameters (i.e., fluxes that are particularly difficult to measure in the VSBL) and it is also not affected by self-correlation (Sorbjan and Grachev 2010).

Further insights into the SBL are crucial for further progress in climate modeling and NWP (Holtslag et al. 2013). Atmospheric circulation models tend to require more drag at the surface than can be justified from local field observations on drag due to vertical shear (Beare 2007; Svensson and Holtslag 2009). This may be due to differences between processes captured by local observations and those acting on the scale of a grid cell, in particular over complex terrain with additional drag resulting from horizontal shear (Goger et al. 2018) or gravity waves (Steeneveld et al. 2008). Without the enhanced drag, the predicted weather systems are typically too persistent. Hence, climate and NWP models have utilized a so-called enhanced mixing approach (Louis 1979) for decades. This approach comes, however, at the cost of the representation of the SBL that is often too warm near the surface, too deep, and the modeled LLJ are often "diluted." This has large consequences for applications such as air quality modeling (Fernando and Weil 2010), road state forecasting (Karsisto et al. 2017), wind energy production (Heppelmann et al. 2017) and visibility forecasts for aviation (Román-Cascón et al. 2019). In climate models, enhanced mixing may result in a positive surface temperature bias (Holtslag et al. 2013), increasing the upwelling longwave radiation (temperature feedback) and decreasing the reflected shortwave radiation through enhanced snow and ice melt (albedo feedback). To overcome the shortcomings of the enhanced mixing approach without impacting the model performance on larger scales, future SBL parameterizations would have to take into account all sources of mechanical drag, for which detailed observations are essential.

A number of earlier field campaigns have been dedicated to SBL studies, either over midlatitude grass fields, such as the Cooperative Atmosphere–Surface Exchange Study in 1999 (CASES-99) in Kansas (Poulos et al. 2002) and Stable Atmospheric Boundary-Layer Experiment in Spain (SABLES 98) in Spain (Cuxart et al. 2000); in hilly terrain with a focus on mountain weather, such as Mountain Terrain Atmospheric Modeling and Observations (MATERHORN) in Utah (Fernando et al. 2015); or in polar regions such as the Surface Heat Budget of the Arctic Ocean (SHEBA) experiment in the Arctic Ocean (Uttal et al. 2002). These studies provided a wealth of observational data and their analysis offered highly valuable insights into SBL behavior. All these campaigns were, however, limited by their in situ measurements being from rather low meteorological masts and with supporting atmospheric profiling, e.g., by radiosondes, having rather poor temporal resolution. The availability of new instruments, observation techniques and measurement platforms for probing the SBL, UAS in particular, now offers unique and unrivaled opportunities for a new generation of polar SBL observations (Kral et al. 2018).

The application of unmanned, at that time remotely controlled, aircraft for atmospheric research, started at the end of the 1960s. Konrad et al. (1970) used a commercially available hobby model airplane with a wingspan of around 2.5 m to measure profiles of temperature and humidity up to 3 km above ground. About two decades later, more systematic attempts for atmospheric investigations were conducted, mainly based on relatively large military drones modified for scientific applications (Langford and Emanuel 1993; Stephens et al. 2000). A breakthrough on the path toward smaller and more cost-efficient systems was the Aerosonde, with a wingspan of 2.9 m, an overall take-off weight of 15 kg, and about 5 kg of scientific payload capacity (Holland et al. 2001).

A rapid development of small airframes, autopilots and meteorological sensors from around 2000 is the direct result of the substantial progress in microelectronics and component miniaturization. One of the pioneering attempts was the still remotely controlled system Kali that performed more than 150 flights in Nepal and Bolivia to investigate thermally driven flows in the Himalayas and the Andes (Egger et al. 2002, 2005). During the following decade, a number of different research groups developed small meteorological UAS systems with the aim of providing reasonably priced airborne sensing capabilities for boundary layer research. Some of the most prominent examples are Small Unmanned Meteorological Observer (SUMO; Reuder et al. 2009), Meteorological Mini Aerial Vehicle (M^2AV; Spiess et al. 2007), Multi-Purpose Airborne Sensor Carrier (MASC; Wildmann et al. 2014), Smartsonde (Chilson et al. 2009; Bonin et al. 2013), and Pilatus (de Boer et al. 2015). A comprehensive overview of small UAS for atmospheric research can be found in Elston et al. (2015).

Many ABL campaigns have relied on UAS based data sampling (e.g., Houston et al. 2012; Reuder et al. 2012b; Bonin et al. 2013; Lothon et al. 2014; Reuder et al. 2016; de Boer et al. 2019). Several of the aforementioned systems have also been operated successfully in polar environments and provided unique profiles of basic meteorological parameters that have been used for process studies (Curry et al. 2004; Cassano et al. 2010; Cassano 2013; Knuth and Cassano 2014; Jonassen et al. 2015; de Boer et al. 2018), mesoscale model validation (Mayer et al. 2012b,c) and the evaluation of the benefit of UAS data assimilation (Jonassen et al. 2012; Sun et al. 2020). However, as fixed-wing systems, they have shortcomings and limitations with respect to accurate measurements in the stable surface layer close to the ground. Rotary-wing multicopter systems, with their ability to hover and to slowly ascend and descend vertically, have here clear advantages (Neumann and Bartholmai 2015; Palomaki et al. 2017; Wrenger and Cuxart 2017; Bell et al. 2020; Segales et al. 2020).

On the basis of previous field campaigns, it is evident that the SBL is often highly heterogeneous over a variety of horizontal scales (e.g., Martínez et al. 2010; Cuxart et al. 2016). Hence, we have to question the classical assumption that sampling over time at one point is equivalent to sampling instantly in space. Accordingly, there is a need for the use of mobile sensor platforms, allowing for observations over a broad range of spatial scales. In ISOBAR we respond to this need by operating a variety of UAS with different capabilities, supported by point and profile observations.

The ISOBAR17 and ISOBAR18 field campaigns

As an integral part of the ISOBAR project, we carried out two field campaigns over the sea ice of the northern Baltic Sea close to the Finnish island Hailuoto in February 2017 and 2018 (see Table 1 for a list of all participants). Hailuoto is located in the Bothnian Bay, the northernmost part of the Baltic Sea, about 20 km west of the city of Oulu (Fig. 1). It covers roughly 200 km^2, with its highest point reaching only about 20 m MSL. Our field site was located at 65.037°N and 24.555°E, just offshore of Hailuoto Marjaniemi, the westernmost point of the island, which is also the location of a WMO weather station, operated by the Finnish Meteorological Institute (FMI). Besides the solid sea ice conditions that can be expected for the Bothnian Bay in February (Uotila et al. 2015), the daylight periods are still relatively short, favoring the VSBL development. In addition, this field site provided a solid infrastructure, easy access and the Finnish air traffic regulations allowed for an unbureaucratic flight permission process that enabled very flexible and science-driven UAS operations during the two campaigns.

The observational setup largely relied on micrometeorological masts installed on the sea ice, a few hundred meters southwest of the FMI weather station (Fig. 1). In 2017 we installed a 4-m mast on the sea ice, equipped with one eddy-covariance (EC) system, three levels of slow-response instrumentation, net radiation and its components (upward and downward for both solar shortwave and thermal longwave radiation), and two ground heat flux sensors.

This setup was extended in 2018 by erecting a 10-m mast (referred to as GFI2), equipped with the same set of sensors and two additional EC systems. An additional 2-m mast (GFI1), consisting of an EC system and a net radiometer, was placed about 65 m to the north-northwest of the 10-m mast. The nearby WMO station provides observations of temperature, humidity, pressure, cloud base height, cloud fraction, visibility, and precipitation every 10 min at a height of 2 m AGL and observations of wind speed, wind direction, and sonic temperature at the height of 46 m MSL. Details on station location, sensor placement and specifications for the two campaigns and the different automatic weather stations are summarized in Table 2.

Table 1. Alphabetic list of campaign participants.

Name	Affiliation	Year
Jan Ahrens	Ostwestfalen-Lippe UASA	2018
Kjell zum Berge	University of Tübingen	2018
Elise Mogster Braaten	University of Bergen	2018
Line Båserud	University of Bergen	2017/18
Phil Chilson	University of Oklahoma	2018
William Doyle	University of Oklahoma	2018
Heidi Midtgarden Golid	University of Bergen	2018
Brian Greene	University of Oklahoma	2018
Kristine Flacké Haualand	University of Bergen	2018
Philipp Hilsheimer	University of Tübingen	2017
Marie Hundhausen	University of Tübingen	2017
Stephan T. Kral	University of Bergen	2017/18
Marius O. Jonassen	University Centre in Svalbard	2017
Carsten Langohr	Ostwestfalen-Lippe UASA	2017/18
Christian Lindenberg	Lindenberg und Müller GmbH and Co. KG	2017/18
Patrick Manz	University of Tübingen	2018
Hasan Mashni	University of Tübingen	2018
Santiago Mazuera	University of Oklahoma	2018
Martin Müller	Lindenberg und Müller GmbH and Co. KG	2017/18
Ewan O'Connor	Finnish Meteorological Institute	2017
Elizabeth Pillar-Little	University of Oklahoma	2018
Alexander Rautenberg	University of Tübingen	2017/18
Joachim Reuder	University of Bergen	2018
Martin Schön	University of Tübingen	2018
Markus Schygulla	University of Tübingen	2017
Antonio Segalés	University of Oklahoma	2018
Andrew Seidl	University of Bergen	2018
Irene Suomi	Finnish Meteorological Institute	2017/18
Gabin H. Urbancic	University of Bergen	2017
Timo Vihma	Finnish Meteorological Institute	2017/18
Hendrik Voss	Ostwestfalen-Lippe UASA	2017/18
Burkhard Wrenger	Ostwestfalen-Lippe UASA	2017/18

For continuous observations of the vertical wind profile and the turbulent structure of the lower atmosphere, we deployed a number of different ABL remote sensing systems: a vertically pointing 1D LATAN-3M sodar in 2017 and 2018 (Kouznetsov 2009; Kral et al. 2018), a Leosphere WindCube 100S (WC100s) scanning wind lidar in 2017 (Kumer et al. 2014; Kral et al. 2018), a 3D Scintec MFAS phased array sodar in 2018, and a 3D Leosphere WindCube v1 (WCv1) Doppler wind lidar in 2018 (Kumer et al. 2014, 2016). Table 3 provides an overview of the specifications of these systems and the observed variables.

Complementing the observations from the stationary systems, we made intensive use of a number of meteorological UAS, in order to sample profiles of the most important thermodynamic and dynamic properties of the ABL and the lower free atmosphere. A summary of the different UAS and their specifications with corresponding references is given in Table 4 and Fig. 2. The three UAS shown in Fig. 2 but not listed in Table 4 were still at an experimental stage and their data were not shown in this article.

For atmospheric profiles of temperature, humidity and wind up to 1,800 m (just below flight level 65, our altitude operation limit defined by the aviation authorities) we used the fixed-wing system SUMO, with repeated profiles every 3–4 h during intensive observational periods (IOPs). Multicopter profiles based on the Bebop2Met (abbreviated B2M), Q13, and

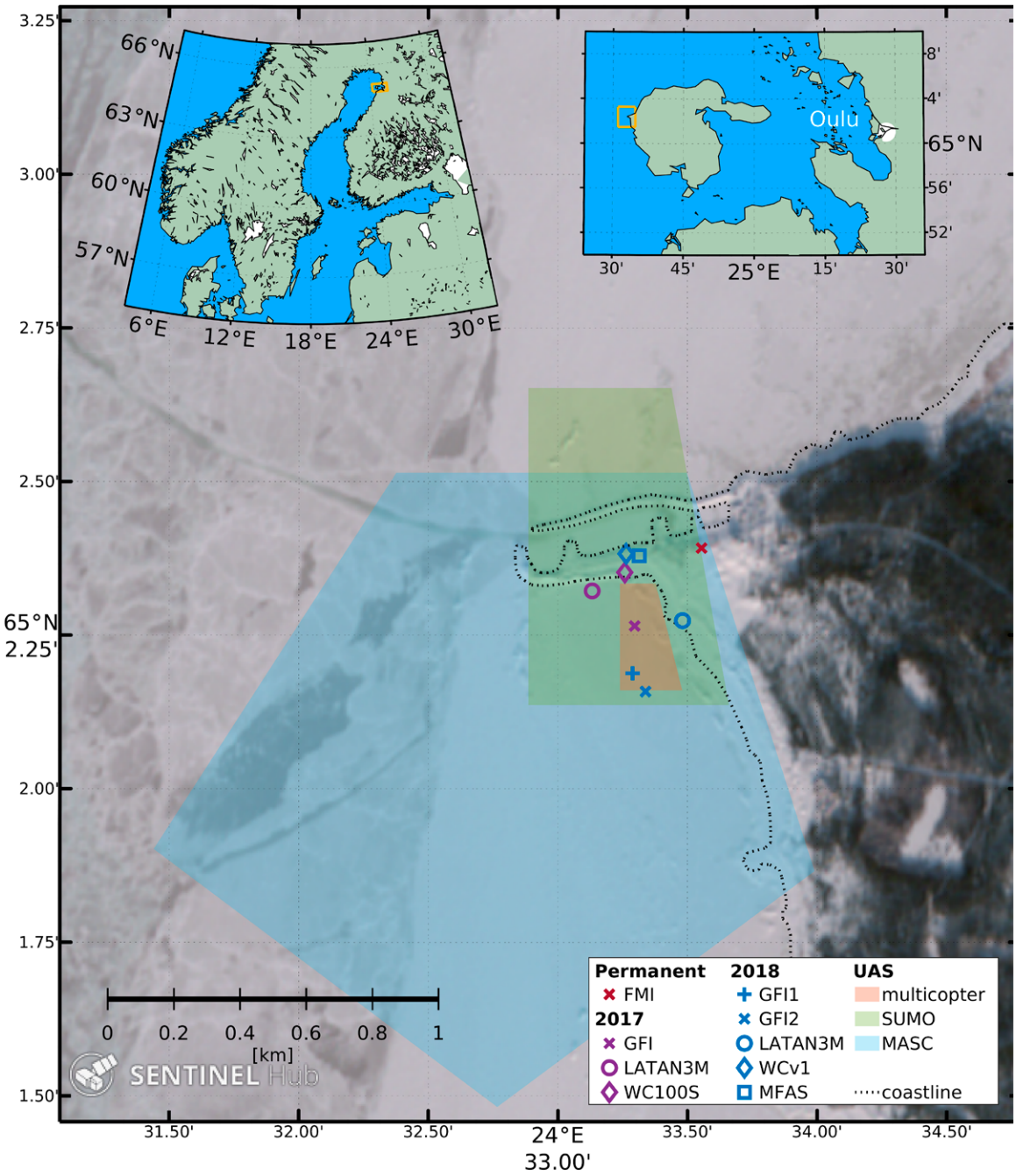

Fig. 1. Overview maps showing the ISOBAR field site: The two inlay maps at the top display the area of Northern Europe (left) and around Hailuoto and Oulu (right). The large map is based on a *Sentinel-2* L2A satellite image from 18 Feb 2019 (https://apps.sentinel-hub.com/eo-browser).

CopterSonde (CS) were carried out roughly every 15–30 min during IOPs to gain profiles of the lowermost 200–300 m at high vertical resolution. To capture prevailing strong gradients within the SBL, we operated the multicopters at fairly low climb rates between 0.5 and 1 m s^{-1}. The second fixed-wing UAS, MASC-2/3, measured turbulence properties along horizontal straight legs at fixed altitudes between 10 and 425 m, vertically separated by 10–25 m. An overview of the different IOPs, including a basic description of the observed conditions and the number of performed UAS flights is given in Table 5.

Postprocessing including thorough quality checks resulted in two extensive datasets on the SBL over sea ice. The overall data availability (see Fig. 3 for an overview for the different systems) was significantly improved for ISOBAR18 compared to the previous year. UAS data availability during the first days of the campaigns is very limited since the preparation of the UAS

Table 2. Specifications of the AWS instrumentation with measured parameters: temperature T; sonic temperature T_s; relative humidity, RH; pressure p; wind components u, v, w; wind speed, ws; wind direction, wd; cloud base height h_{CB} and fraction CF; SYNOP weather codes, syn; precipitation, prec; visibility, vis; H_2O and CO_2 concentration; up- and downwelling short- and longwave radiation, $SW^{\uparrow\downarrow}$, $LW^{\uparrow\downarrow}$; ground heat flux, GF.

AWS	Parameters	Sensor	Acquisition period	Measurement height
FMI (2017/18); 65.0399°N, 24.5592°E	T, RH	Vaisala HMP155	10 min	2.0 m AGL (9 m ASL)
	p	Vaisala PTB 201 A	10 min	7 m ASL
	T	Pentronic AB Pt100	10 min	2.0 m AGL (9 m ASL)
	ws, wd, T_s	Adolf Thies UA2D	1 s	38.5 m AGL (45.5 m ASL)
	h_{CB}, CF	Vaisala CT25K Laser Ceilometer	10 min	
	syn, prec, vis	Vaisala FD12P Weather Sensor	10 min	
GFI (2017); 65.0378°N, 24.5549°E	T	Campbell ASPTC (aspirated)	1 min	1.0, 2.0, 4.0 m AGL
	T	PT100 (aspirated)	1 min	1.0, 2.0, 4.0 m AGL
	RH	Rotronic HC2-S (aspirated)	1 min	1.0, 2.0, 4.0 m AGL
	ws	Vector A100LK	1 min	1.0, 2.0, 4.0 m AGL
	wd	Vector W200P	1 min	1.0, 2.0, 4.0 m AGL
	$SW^{\uparrow\downarrow}$, $LW^{\uparrow\downarrow}$	Kipp and Zonen CNR1	1 min	1.0 m AGL
	GF	Hukseflux HFP01	1 min	Snow and ice
	u, v, w, T_s	Campbell CSAT-3	0.05 s	2.7 m AGL
	H_2O, CO_2, p	LI-COR LI7500	0.05 s	2.7 m AGL
GFI1 (2018); 65.0365°N, 24.5548°E	T	Campbell ASPTC (aspirated)	1 s	2.0 m AGL
	$SW^{\uparrow\downarrow}$, $LW^{\uparrow\downarrow}$	Kipp and Zonen CNR1	1 s	1.0 m AGL
	u, v, w, T_s	Campbell CSAT-3	0.05 s	2.0 m AGL
	H_2O, CO_2, p	LI-COR LI7500	0.05 s	2.0 m AGL
GFI2 (2018); 65.0360°N, 24.5556°E	T	Campbell ASPTC (aspirated)	1 s	0.6, 2.0, 6.8 m AGL
	T	PT100 (aspirated)	1 s	1.0, 2.0, 4.0 m AGL
	RH	Rotronic HC2-S (aspirated)	1 s	1.0, 2.0, 4.0 m AGL
	ws	Vector A100LK	1 s	1.0, 2.0, 4.0 m AGL
	wd	Vector W200P	1 s	1.0, 2.0, 4.0 m AGL
	$SW^{\uparrow\downarrow}$, $LW^{\uparrow\downarrow}$	Kipp and Zonen CNR1	1 s	6.4 m AGL
	GF	Hukseflux HFP01	Snow and ice	
	u, v, w, T_s	Campbell CSAT-3	0.05 s	2.0, 4.6, 10.3 m AGL
	H_2O, CO_2, p	LI-COR LI7500	0.05 s	2.0 m AGL

Table 3. Remote sensing systems specifications with measured parameters as in Table 2 and radial wind speed u_{rad}; standard deviation of wind velocity components σu, σv, σw; attenuated backscatter signal strength, bsc; carrier to noise ratio, CNR.

Instrument	Type	Parameters	Range	Resolution	Acquisition period
LATAN-3M (2017/18)	1D sodar	w, σw, bsc	10–340 m AGL	10 m (vertical)	3 s
WindCube 100S (2017)	3D scanning Doppler lidar	U_{rad}, CNR	50–3,300 m (radial)	25 m (radial)	1 s
WindCube v1 (2018)	3D Doppler lidar	u, v, w, σu, σv, σw, CNR	40–250 m AGL	20 m (vertical)	4 s
MFAS (2018)	3D sodar	u, v, w, σw, bsc	40–1,000 m AGL	10 m (vertical)	10 min

was started after the installation of most ground-based systems was finished. The UOWL team operating the Q13 UAS could not participate for the full campaign period and decided to focus on the last week of ISOBAR17 and the last two weeks of ISOBAR18. In addition, the Bebop2Met (in 2017) and the CopterSonde (in 2018) were operated for the first time during a scientific campaign and required extensive preparation, resulting in limited data availability from these UAS during approximately the first week of the corresponding campaign. Furthermore, icing

Table 4. UAS specifications with measured parameters as in Table 2 and infrared temperature T_{IR}. In addition to the listed sensors each UAS is equipped with a GNSS to measure the aircraft's position (latitude, lat; longitude, lon; altitude, alt) and an IMU for the aircraft's attitude angles (pitch θ; roll φ; yaw ψ). See listed references for more detailed information.

UAS	Operator	Parameter	Sensor	Acquisition frequency	Reference
SUMO (fixed wing)	GFI	T, RH	Sensirion SHT75	2 Hz	Reuder et al. (2009)
		T	Pt1000 Heraeus M222	8.5 Hz	Reuder et al. (2012a)
		p	MS 5611	4 Hz	
		T_{IR}	MLX90614	8.5 Hz	
		ws, wd	Aircraft Dynamics	4 Hz	
Bebop2Met (rotary wing)	GFI	T, RH	Sensirion SHT75	2 Hz	Kral et al. (2018)
		p	MS 5607	0.77 Hz	
		ws, wd	Aircraft Dynamics	4 Hz	
Q13a (rotary wing)	UOWL	T, RH	HYT 271	10 Hz	Wrenger and Cuxart (2017)
		p	BMP 180	10 Hz	
		ws	Modern Device Wind Sensor Rev. P	10 Hz	
Q13b (rotary wing)	UOWL	T, RH	HYT 271	10 Hz	Wrenger and Cuxart (2017)
		T	K-type thermocouple 25 μm	10 Hz	
		p	BMP 180	10 Hz	
		T_{IR}	MLX90614	10 Hz	
CopterSonde (rotary wing)	OU	T	iMet XF PT 100	10 Hz	Greene et al. (2019)
		T, RH	HYT 271	10 Hz	Segales et al. (2020)
		p	Pixracer barometer	10 Hz	
		ws, wd	Aircraft Dynamics	10 Hz	
MASC-2/3 (fixed wing)	UT	T	Pt-fine-wire	100 Hz	Wildmann et al. (2014)
		T, RH	Sensirion SHT31	10 Hz	Rautenberg et al. (2019)
		RH	P14 Rapid	10 Hz	
		p	HCA-BARO	100 Hz	
		u, v, w	Custom 5-hole probe	100 Hz	

on the inside of the WindCube 100S lens (in 2017) and the late arrival of the WindCube v1 (in 2018) caused the major data gaps in the remotely sensed wind profiles.

Meteorological and sea ice conditions

ISOBAR17 was exposed to varying weather conditions (Fig. 4a). Around the start of the campaign, a large high pressure pattern strengthened over Finland, resulting in a few days with clear skies and cold temperatures. From mid-February and onward, several low pressure systems passed Scandinavia and Finland,

Fig. 2. The different UAS systems used during the two campaigns. The numbers of flights are indicated in parentheses for ISOBAR17 and ISOBAR18, respectively.

Table 5. List of IOPs during ISOBAR17 and ISOBAR18, summarizing the observed ABL conditions (i.e., stability regime, wind regime, relevant phenomena, and maximum near-surface vertical temperature difference and lapse rate) and the corresponding large-scale conditions [i.e., average wind speed and direction (850–925 hPa); subsidence $\bar{\omega}$; horizontal temperature advection (adv); cloud cover; and synoptic situation]. Additional information on the evolution of the large-scale conditions is given in parentheses. The large-scale conditions are extracted from ERA5 reanalysis data (Hersbach et al. 2020).

IOP No.	Start date/time	End date/time	Boundary layer conditions	Large-scale conditions	No. of UAS flights
1	1500 UTC 14 Feb 2017	0630 UTC 15 Feb 2017	Near neutral to very stable; light to calm winds; $\Delta T_{4-1m} = 3.8$ K ($\Lambda = 1.3$ K m^{-1})	6 (11–4) m s^{-1} NNW (NNW–WSW); $\bar{\omega} = 0.07$ Pa s^{-1}; adv = 0.01 K h^{-1}; broken cloud cover; high pressure ridge	15
2	2300 UTC 20 Feb 2017	0600 UTC 21 Feb 2017	Near neutral; moderate winds; $\Delta T_{4-1m} = 0.8$ K ($\Lambda = 0.3$ K m^{-1})	10 (9–11) m s^{-1} NNW; $\bar{\omega} = 0.07$ Pa s^{-1}; adv = 0.13 K h^{-1}; clear sky; weak eastward-propagating trough	13
3	1700 UTC 21 Feb 2017	2300 UTC 21 Feb 2017	Partially very stable; calm to light winds; $\Delta T_{4-1m} = 6.4$ K ($\Lambda = 2.1$ K m^{-1})	10 (6–18) m s^{-1} SSW (NW–S); $\bar{\omega} = 0.02$ Pa s^{-1}; adv = −0.06 K h^{-1}; scattered clouds; weak eastward-propagating trough	9
4	0400 UTC 25 Feb 2017	1100 UTC 25 Feb 2017	Near neutral; moderate winds; $\Delta T_{4-1m} = 0.5$ K ($\Lambda = 0.2$ K m^{-1})	13 (14–12) m s^{-1} NNW; $\bar{\omega} = 0$ Pa s^{-1}; adv = 0.56 K h^{-1}; clear sky; low pressure influence	24
5	0200 UTC 26 Feb 2017	0730 UTC 26 Feb 2017	Near neutral to weakly stable; moderate winds; rapid cooling (~10 K in 3 h); $\Delta T_{4-1m} = 0.3$ K ($\Lambda = 0.1$ K m^{-1})	6 (9–4) m s^{-1} NNW; $\bar{\omega} = 0.01$ Pa s^{-1}; adv = −0.12 K h^{-1}; scattered clouds; weak trough	23
6	1400 UTC 26 Feb 2017	0200 UTC 27 Feb 2017	Near neutral to very stable; light to calm winds; wave breaking (Kelvin–Helmholtz billows); $\Delta T_{4-1m} = 0.62$ K ($\Lambda = 2.1$ K m^{-1})	5 (6–4) m s^{-1} NNE; $\bar{\omega} = 0.08$ Pa s^{-1}; adv = 0.16 K h^{-1}; clear sky; weak pressure gradients	32
7	1130 UTC 10 Feb 2018	0100 UTC 11 Feb 2018	Near neutral to weakly stable; moderate winds; $\Delta T_{6.9-0.6m} = 3.2$ K ($\Lambda = 0.5$ K m^{-1})	13 (17–8) m s^{-1} SW; $\bar{\omega} = 0.06$ Pa s^{-1}; adv = 0.47 K h^{-1}; overcast, intermittent clear sky periods; strong pressure gradient (decreasing)	13
8	0500 UTC 16 Feb 2018	0400 UTC 17 Feb 2018	Near neutral to weakly stable; elevated inversion > 50 m; LLJ; $\Delta T_{6.9-0.6m} = 1.5$ K ($\Lambda = 0.2$ K m^{-1})	2 (4–1) m s^{-1} S (SE–SW); $\bar{\omega} = 0.06$ Pa s^{-1}; adv = 0.05 K h^{-1}; broken cloud cover; weak pressure ridge	28
9	1400 UTC 17 Feb 2018	0230 UTC 18 Feb 2018	Weakly to very stable; light to calm winds; $\Delta T_{6.9-0.6m} = 5.6$ K ($\Lambda = 0.9$ K m^{-1})	2 (3–2) m s^{-1} NE; $\bar{\omega} = 0.01$ Pa s^{-1}; adv = 0.01 K h^{-1}; clear sky to overcast; weak high pressure ridge	38
10	1330 UTC 18 Feb 2018	0230 UTC 19 Feb 2018	Weakly to very stable; very light to calm winds; LLJ (upside-down mixing); wave breaking; $\Delta T_{6.9-0.6m} = 5.1$ K ($\Lambda = 0.8$ K m^{-1})	5 (4–6) m s^{-1} NNE; $\bar{\omega} = 0.03$ Pa s^{-1}; adv = − 0.23 K h^{-1}; overcast, intermittent clear sky periods; high pressure influence (developing)	45
11	1500 UTC 19 Feb 2018	2200 UTC 19 Feb 2018	Weakly stable; moderate winds; LLJ; $\Delta T_{6.9-0.6m} = 3.5$ K ($\Lambda = 0.5$ K m^{-1})	6 (8–5) m s^{-1} ENE; $\bar{\omega} = 0.1$ Pa s^{-1}; adv = 0.15 K h^{-1}; clear sky; high pressure influence	14
12	1100 UTC 20 Feb 2018	0600 UTC 21 Feb 2018	Near neutral to very stable; light winds; elevated inversion 100 to 180 m; $\Delta T_{6.9-0.6m} = 5.4$ K ($\Lambda = 0.9$ K m^{-1})	2 (2–3) m s^{-1} N (NE–NW); $\bar{\omega} = 0.01$ Pa s^{-1}; adv = 0.01 K h^{-1}; overcast, clear sky after 0400 UTC; high pressure influence	51
13	0500 UTC 22 Feb 2018	1800 UTC 22 Feb 2018	Near neutral to weakly stable; light winds; $\Delta T_{6.9-0.6m} = 2.1$ K ($\Lambda = 0.3$ K m^{-1})	6 (5–7) m s^{-1} N; $\bar{\omega} = -0.06$ Pa s^{-1}; adv = 0.19 K h^{-1}; broken cloud cover; clear sky after 1200 UTC; high pressure influence	9
14	1300 UTC 23 Feb 2018	0600 UTC 24 Feb 2018	Weakly to very stable; light winds; LLJ; waves; $\Delta T_{6.9-0.6m} = 4.3$ K ($\Lambda = 0.7$ K m^{-1})	6 (6–5) m s^{-1} NE; $\bar{\omega} = 0.14$ Pa s^{-1}; adv = −0.17 K h^{-1}; clear sky, intermittent scattered cloud cover; high pressure influence	44

causing high variations in wind speed and direction. From 24 February on, the Bothnian Bay was again under the influence of high pressure, creating favorable conditions for SBL development. Relatively, the temperature was mostly mild, with only few days below −10°C. Consistent with the mild weather, the sea ice extent of the Baltic sea in February 2017 was considerably smaller than usual (compared to a reference period of 2006–18, not shown). The sea ice concentration in the Bothnian Bay grew rapidly from 5 to 12 February (Figs. 4b,c)

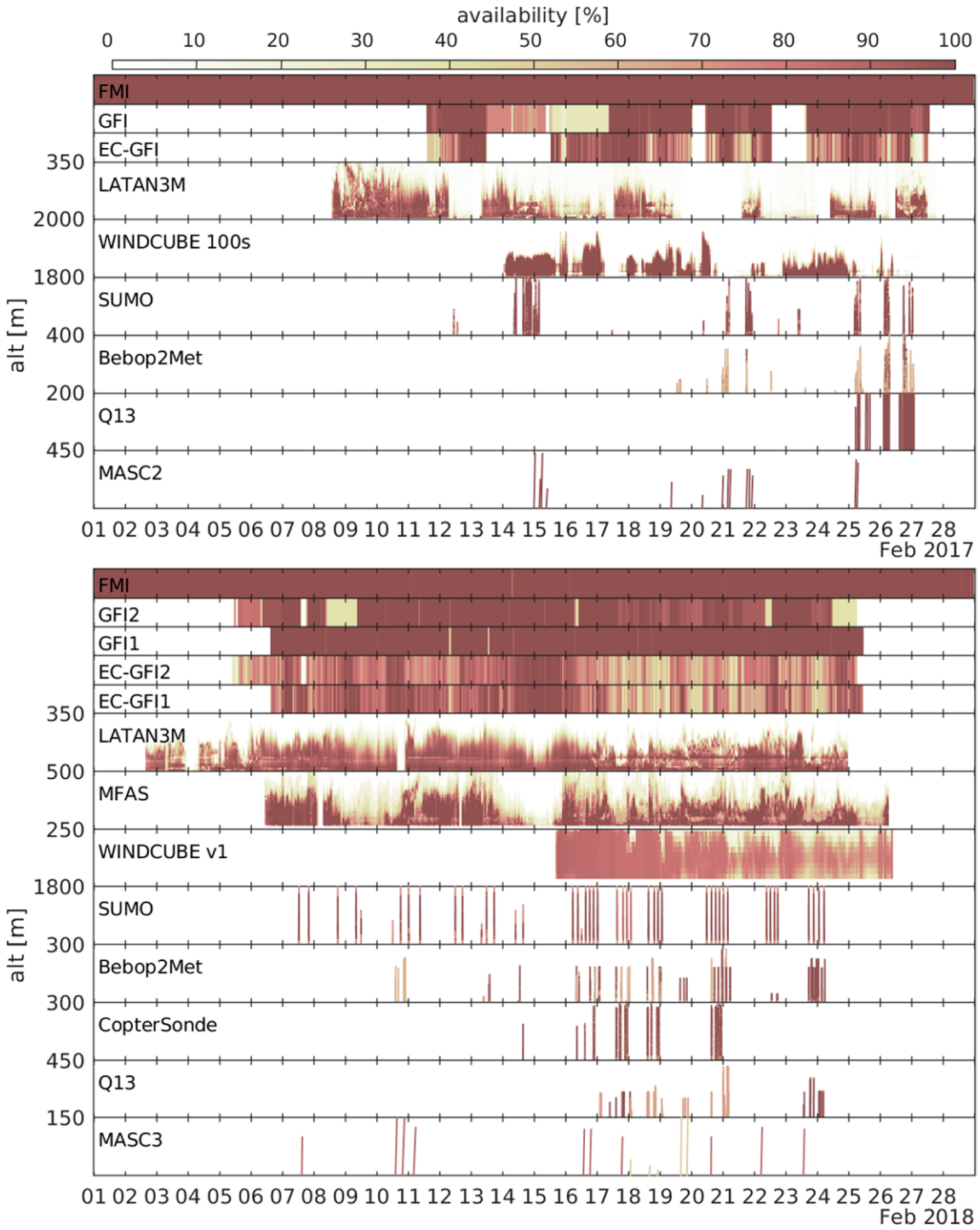

Fig. 3. Data availability for the measurement systems during the ISOBAR17 and ISOBAR18 campaigns. For the profiling systems the data availability is given as a function of height.

during the relatively cold period associated with the high pressure system in the beginning of the campaign. From mid-February, the large-scale flow packed the ice toward the northeast of the Bothnian Bay, resulting in a local minimum in the sea ice concentration on 18 February (Fig. 4d). Afterward, the sea ice concentration gradually increased until the end of the month (Fig. 4e).

In contrast to the varying synoptic conditions the year before, the weather during ISOBAR18 was dominated by high pressure (Fig. 4f). In February 2018 temperatures were low, winds were relatively weak and mostly from the north and there were many days with clear skies. An exception to these meteorological conditions occurred during the passage of a low pressure

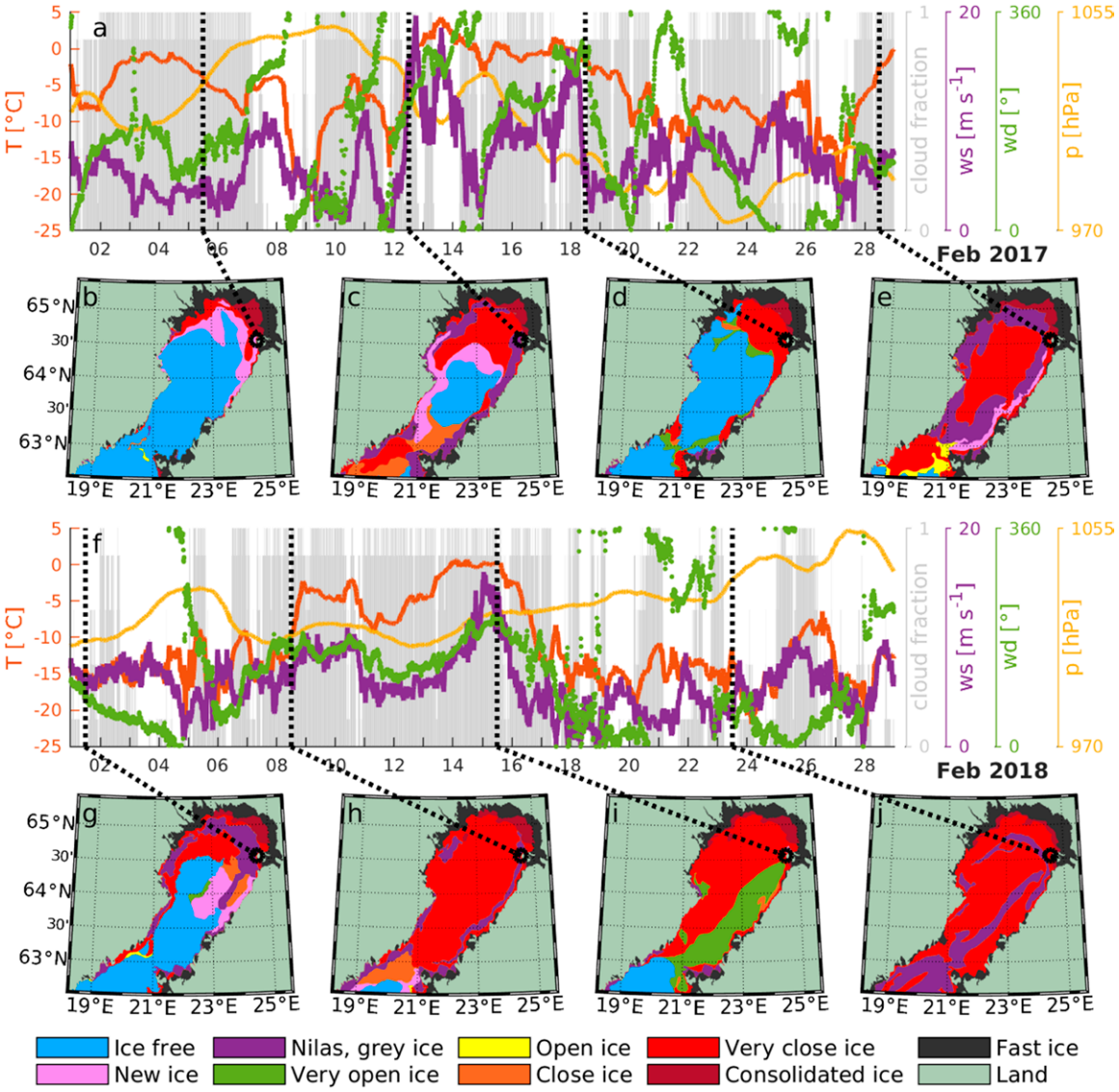

Fig. 4. Overview of the meteorological and sea ice conditions during the two campaigns in February 2017 and 2018. (a),(f) The time series of temperature, cloud cover, wind speed and direction, and pressure observed by the WMO weather station (FMI) during February 2017 and 2018, respectively. (b)–(e),(g)–(j) The ice charts in represent the extrema of the ice coverage during the corresponding period based on data provided by the Finnish Meteorological Institute. Black dotted lines indicate the time of observation and the corresponding location on the maps.

system from the North Sea toward northern Sweden and Finland around 8–16 February, resulting in strong southerly winds and temperatures up to 0°C. Before and after this period, daily mean temperatures were typically below –10°C and the wind speed was mostly low to moderate. The high pressure blocking situation during ISOBAR18 is consistent with a colder sea ice season compared to ISOBAR17, with gradually increasing sea ice concentration and thickness during the cold periods of 1–8 February (Figs. 4g,h) and 15–23 February (Figs. 4i,j). The Bothnian Bay was more or less ice covered throughout the ISOBAR18 campaign.

Overall, the sea ice conditions and weather situation were more favorable for the formation of VSBL during ISOBAR18. An overview of the large-scale and corresponding boundary layer conditions during the 14 IOPs is provided in Table 5.

Synthesis of UAS and ground-based in situ and remote sensing observations

The two ISOBAR field campaigns comprised a variety of observation systems, thus the synthesis of observations on the basic meteorological parameters, such as wind speed, direction,

temperature and humidity, required carefully designed postprocessing procedures. In particular the UAS data underwent procedures for sensor calibration, reprocessing of altitude data based on observed pressure and air temperature instead of assuming a standard atmosphere lapse rate, response time correction (UAS thermodynamic parameters) and QA/QC procedures, especially for the wind estimation algorithms. Excellent examples for the quality of this synthesis are the profiles from 1510 to 1530 UTC 20 February 2018 when all four profiling UAS (SUMO, B2M, CS2, and Q13) were operated quasi-simultaneously together with the ground-based observations from GFI2, FMI, MFAS and WCv1. The resulting profiles in Fig. 5, reveal a very good agreement between the different systems. All UASs and the 10-m mast sample a well-mixed layer up to ~100 m topped by a sharp inversion. The observed wind speed profiles also agree very well with light winds below 2 m s^{-1} in the lowermost 60 m and increasing wind speeds up to 4–5 m s^{-1}, peaking at about 200 m. CopterSonde, lidar (WCv1) and sodar (MFAS) show slightly higher wind speeds at this level with the CopterSonde indicating this being related to a LLJ. The SUMO did not reproduce the same peak wind speed at this level, as its wind estimation algorithm (Mayer et al. 2012a) takes data over one full circular flight track into account, which results in a smoother wind profile. Furthermore, the presented wind speed profiles from MFAS and WCv1 represent 30-min averages, whereas UAS profiles are based on quasi-instantaneous observations.

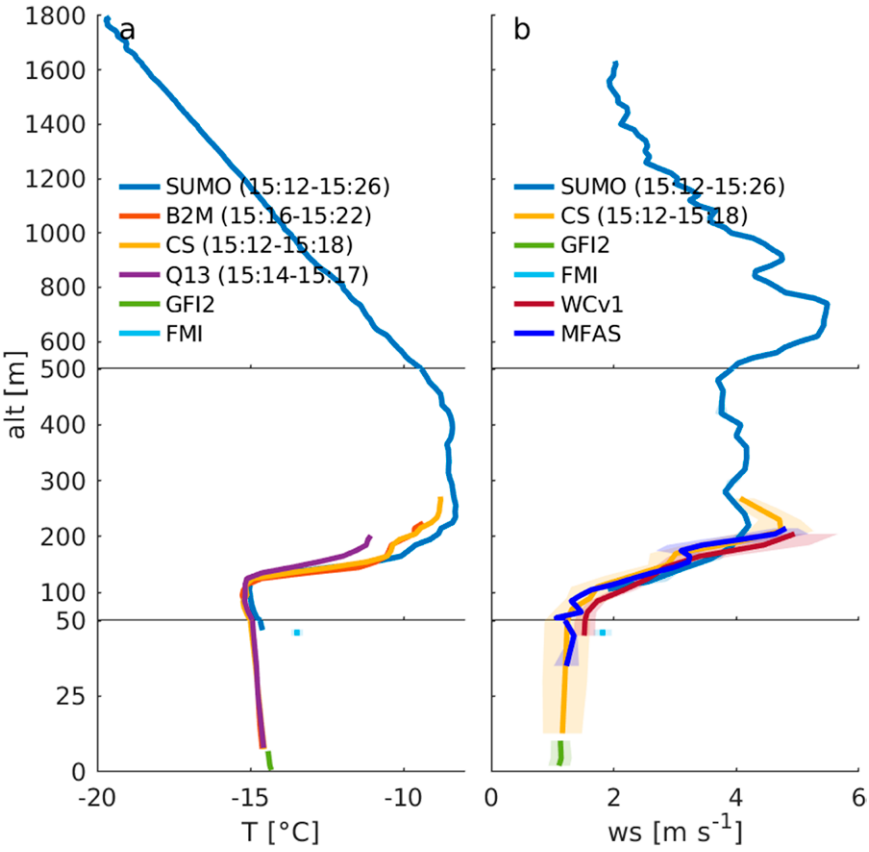

Fig. 5. Combined temperature *T* and wind speed (ws) profiles based on mast, UAS, and remote sensing (wind only) data, observed between 1510 and 1530 UTC 23 Feb 2018. Solid lines and shaded areas indicate the mean and standard deviation (bin averaged for all UAS and time averaged for ground based systems), respectively. The observation period for the ground-based systems is from 1510 to 1530 UTC, and the slightly shorter periods for the UAS flights are given in the legends.

Science highlights

SBL evolution. During IOP-14, 1615–2030 UTC 23 February 2018, UAS based atmospheric profiling with high temporal resolution gives detailed insight into the temporal evolution of the SBL at a spatial resolution on the order of 1 m. This allows for the direct capture of a considerable portion of the turbulent fluctuations, in particular at higher levels, as the size of turbulent eddies is expected to increase with height. Hailuoto was located at the southeastern flank close to the center of the high pressure system and under the influence of weak northeasterly flow (Table 3). Clear-sky conditions favored the development of an SBL, transitioning between the weakly stable and very stable regime. Temperature profiles from the three UAS operated during this IOP, i.e., SUMO, B2M and Q13, indicate an overall cooling of the ABL associated with strengthening

of the surface-based inversion and increase in inversion depth (Fig. 6a). The corresponding near-surface temperature observations (Fig. 6b) confirm the trend of surface cooling and intensification of the inversion, which is initiated by longwave radiative cooling after sunset. Various UAS profiles indicate remarkable, finescale structures of thermal instabilities in layers between the surface and approximately 70 m. In particular, the profiles at 1718, 1741, and 1819 UTC consistently resemble these features. At the same time, we observe a series of rapid temperature changes, most pronounced at the 0.6- and 2.0-m levels. During the cold episodes, the near-surface wind directions change from about 60° to 10° and exhibit a signature of wind veer resembling an Ekman spiral (Fig. 6b). The observed shift in wind direction occurs, however, on time scales much shorter than expected from pure Ekman adjustment, indicating the importance of local advective processes. With the geostrophic wind shifting gradually from roughly 60° to 100°, this results in a surface angle of at least 50°. Note that NWP models in the first GEWEX Atmospheric Boundary Layer Study (GABLS1) show roughly a surface angle of 30° (Svensson and Holtslag 2009), while theory of Nieuwstadt (1985) predicts 60°. The period from about 1815 until 2000 UTC is characterized by a strong surface inversion and meandering of the flow can be observed at all levels up to 46 m. The second weather station on the sea ice (GFI-1, not shown) recorded a very similar temperature and wind signal; however, the changes occur a couple of minutes earlier and the cold periods last longer. Based on these observations, we conclude that these events are related to the passage of microfronts (i.e., the advection of airmasses with different properties). The measured wind direction suggests the warmer airmass being modified by the presence of land, whereas the colder air originates from a rather clean sea ice fetch. The observed finescale instabilities in the vertical profiles lead us to the hypothesis that these microfronts are rather irregular in their shape, potentially triggered by directional shear.

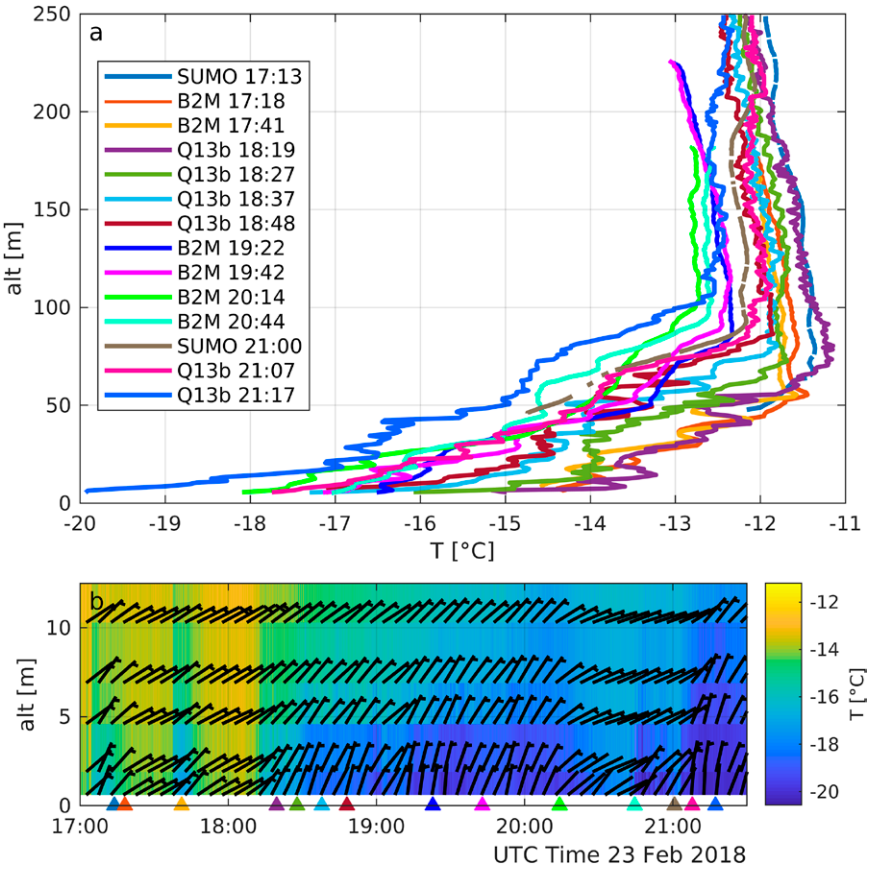

Fig. 6. Series of (a) UAS boundary layer profiles and (b) corresponding time series of surface based measurements of *T* (contours) and ws (wind barbs), observed during IOP-14, 1615–2130 UTC 23 Feb 2018. The UAS flight times for the data presented in (a) (ascent up to 250 m) are indicated by colors, and additional markers in (b), applying the corresponding color scheme.

Disentangling the complexity of the SBL. During IOP-10, 18–19 February 2018, ground-based in situ and remote sensing systems alongside UAS captured a variety of SBL phenomena during two major periods with very stable stratification, the first of which was from 1330 to 1615 UTC while the second was from about 1930 to 0040 UTC. The large-scale situation was characterized by a high pressure system forming in the Barents Sea and associated weak pressure gradients at its southeastern flank, but varying cloud cover (Table 5). The start of

these periods corresponds well with strongly negative net radiation (indicated as colored shading at the top of Fig. 7a), due to clear sky conditions. The temperatures observed at GFI2 (10-m mast on the sea ice) and FMI (permanent 46-m tower) reveal strong vertical gradients during the VSBL cases and are subject to rapid variations, especially at the 4.5- and 6.9-m levels. The LATAN-3M sodar echogram indicates a surface-based turbulent layer extending to a maximum altitude of roughly 100 m, but frequently as shallow as 20 m (or even lower) and with occasional elevated turbulent layers above (Fig. 7c). The wind profile above the ABL is fairly constant with a weak flow from east-northeast (wind barbs in Fig. 7d). Within the ABL, the wind profile is, however, influenced by a variety of processes (e.g., LLJ or submesoscale motions) resulting in strong variability in both wind direction and magnitude (Fig. 7b). In general, IOP-10 was characterized by near-calm conditions, with 31% (63%) of the 10-min averaged 2-m wind speed below 0.5 m s^{-1} (1.0 m s^{-1}), which makes the SBL susceptible to sporadic mixing events generated by wave-like and other submesoscale motions (Mahrt 2011). In the following paragraphs we will highlight some of the observations during the subintervals I–III. The complexity of these cases (i.e., nonlinear interactions between a variety of different scales, including turbulent and nonturbulent motions) is likely to cause severe problems not only in state-of-the-art NWP but also in other atmospheric research models (e.g., Fernando and Weil 2010; Sun et al. 2015).

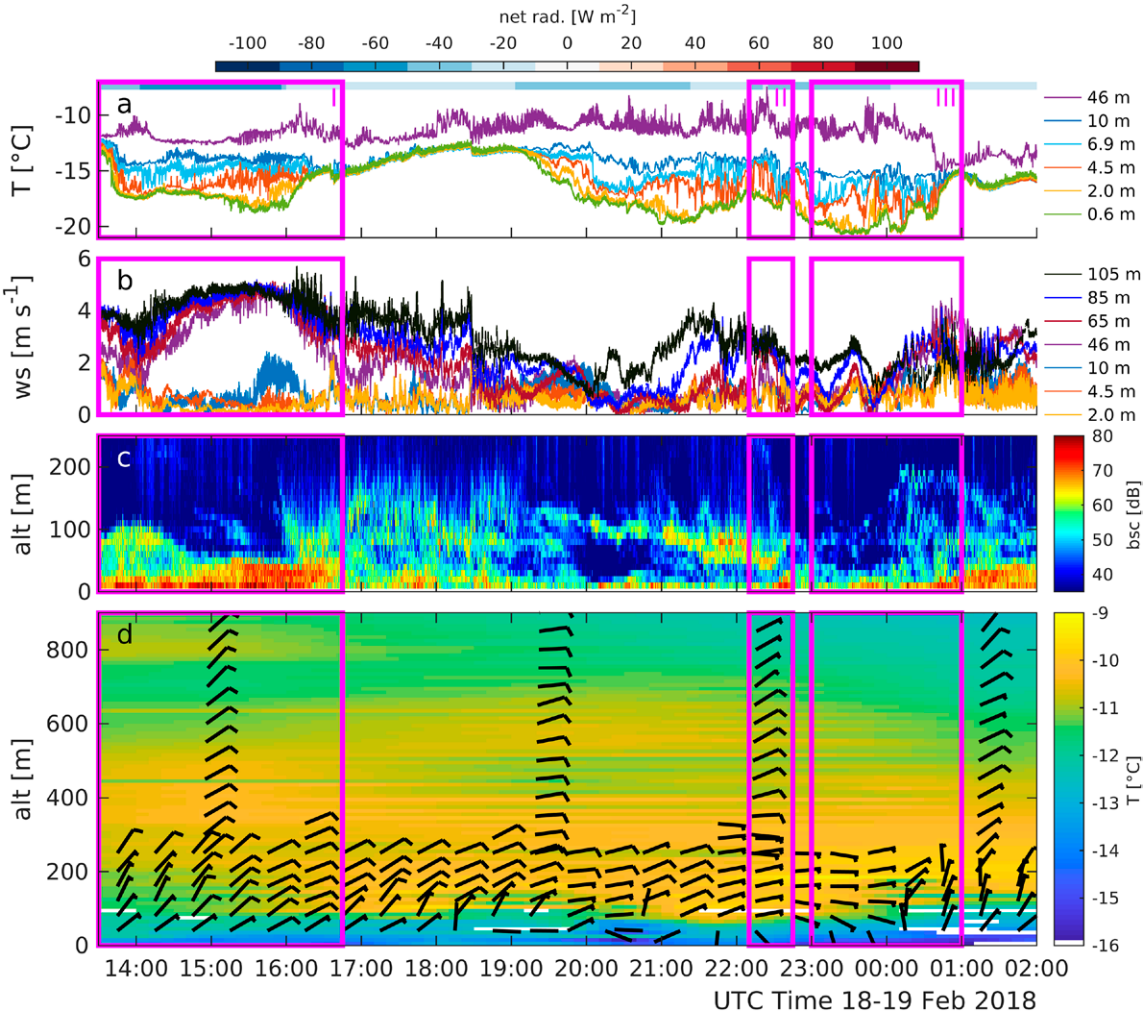

Fig. 7. Time series of various atmospheric parameters during IOP-10, 18–19 Feb 2018: (a) *T* (observed by GFI2 and FMI); (b) ws (GFI2, FMI, and WCv1); (c) sodar attenuated backscatter (bsc) profiles (LATAN-3M); (d) composite profiles of *T* (UAS, GFI2) and horizontal wind (SUMO, WCv1, MFAS). Magenta boxes indicate the periods of interest analyzed in the following figures.

IOP-10/I, INTENSIFICATION AND COLLAPSE OF THE LLJ. The first VSBL interval is initiated by a rapid temperature drop close to the surface of 2 K within 20–30 s (Fig. 8a), accompanied by a reduction in wind speed (Fig. 8b) and a wind direction shift of 180° from north to south (Fig. 8c). During the following minutes (until ~1400 UTC) the near-surface winds almost completely calm down, thus increasing the dynamic stability, while the flow at elevated layers around 100 m slightly accelerates and forms a weak LLJ. All three EC systems of GFI2 show weak intermittent turbulence during this period (see w' in Fig. 8d and $\overline{w'T'}$ in Fig. 8e). Nevertheless, the lowest layers remain at a rather constant temperature; the reason for this is not quite clear. Our mast observations, however, show small-scale oscillations in wind speed and direction at the three lowest levels, which seem rather independent of each other. Occasionally, the

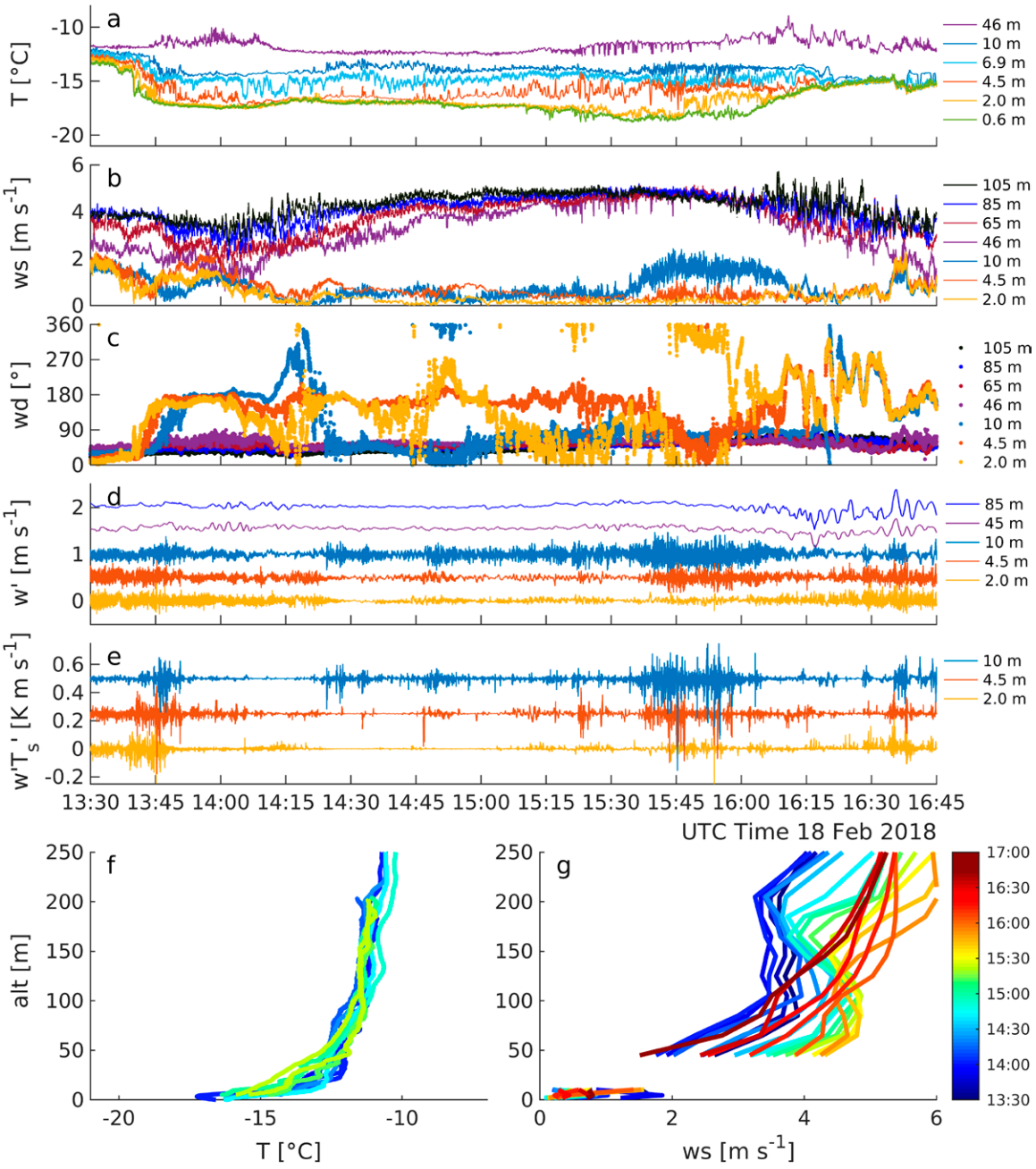

Fig. 8. Time series of various atmospheric parameters during IOP-10, 1330–1615 UTC 18 Feb 2018: (a) T (observed by GFI2 and FMI); (b) ws (GFI2, FMI, and WCv1); (c) wind direction (wd) (GFI2, FMI, and WCv1); (d) vertical velocity perturbation w' (GFI2, WCv1); (e) instantaneous kinematic heat flux $\overline{w'T'}$ (GFI2); (f) vertical profiles of T (UAS); (g) vertical profiles of ws (GFI2, WCv1). The w' and $\overline{w'T'}$ data are shifted by increments of 0.5 m s^{-1} and 0.25 K m s^{-1}, respectively, to reveal structures.

local wind and directional shear might be large enough to trigger small-scale mixing events.

At about 1535 UTC, the 10-m wind speed accelerates to about 2 m s^{-1} triggering a strong intermittent event, which also influences the two EC levels below, although to a weaker extent. Investigating the evolution of the vertical wind profile (Fig. 8g) based on WCv1 lidar and 10-m mast data, suggests that the acceleration of the 10-m wind is related to an increase in wind shear due to the intensification and lowering of the LLJ; eventually this causes a shear instability. The sodar echogram (Fig. 7c) supports this interpretation, as it indicates an elevated weak turbulent layer merging with lower levels around 1440 UTC, followed by an increase in turbulence below 80 m and the lowering of the elevated inversion layer (Fig. 8f). After this event, the wind speed profiles take a more logarithmic shape again. The vertical temperature profiles in Fig. 8f also feature a shift from a very shallow and strong surface-based and an additional elevated inversion to a more logarithmic profile after this event. A reduction in radiative cooling due to increased cloud cover initiates the end of this VSBL period.

IOP-10/II, NEAR-SURFACE WAVE INSTABILITY. During IOP-10 the instrumentation on the 10-m mast recorded a series of amplifying temperature oscillations, most pronounced at 4.5, 6.9, and 10.3 m (Fig. 9a). At 2234 UTC this oscillation results in a remarkable cooling of the 10.3-m temperature, dropping by 4 K within approximately 1 min. Associated with this main cooling event is a temporary shift to neutral static stability and enhanced near surface turbulence

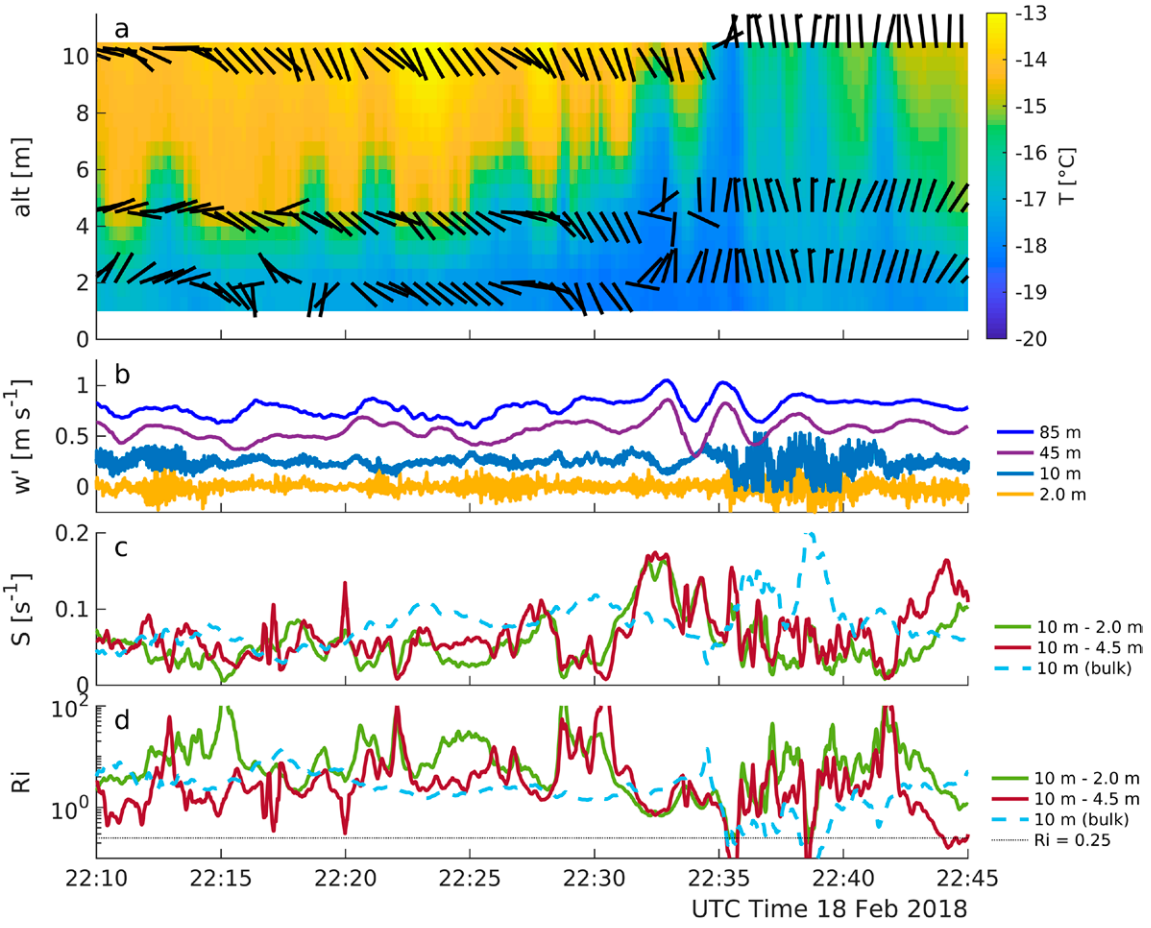

Fig. 9. Time series of various atmospheric parameters during IOP-10, 2210–2245 UTC 18 Feb 2018: (a) temperature *T* (contours) and wind speed and direction (wind barbs), observed by GFI2; (b) vertical velocity perturbation *w′* (GFI2, WCv1); (c) wind shear *S* (GFI2); (d) Richardson number Ri (GFI2). The *w′* data are shifted by increments of 0.25 m s^{-1} to reveal structures. Wind speed at all levels and *w′* data at the upper two levels are smoothed applying a 1-min sliding mean average; *T*, *S*, and Ri data are 10-s sliding mean averages.

(Fig. 9b). The near-surface stability before this event was characterized by a sharp temperature gradient, $\Delta T_{10-0.6\mathrm{m}} \approx 4.5$ K and weak winds at about 1 m s^{-1}, meandering between south-southwest and north-northeast (Fig. 9a). The three sonic anemometers of GFI2 sampled very weak to intermittent turbulence (Fig. 9b), whereas the remote sensing systems (e.g., 45- and 85-m lidar levels in Fig. 9b) indicate some wave activity aloft (see also Fig. 7b). The signature of this wave can also be detected in the 10-m vertical velocity data.

From 2232 UTC the wind at the lowermost levels shifts to a northerly direction, whereas at 10 m it stays south-southeast for two more minutes. This results in enhanced local shear as shown in Fig. 9c, while the bulk shear is still fairly weak. At the same time, the amplitude of the wave starts to grow rapidly, causing an upward transport of cold, near-surface air at the wave crest at 2233 UTC. This is also associated with a shift to near-neutral stratification as reflected in the substantial drop in the gradient Richardson number (Fig. 9d). During the next wave trough, the static stability becomes stable again but the directional shear remains. The following wave crest results in the aforementioned strong elevated cooling event, contributing to further destabilization of the surface layer (Fig. 9d) and the breaking of the wave at 2234 UTC. This wave instability causes enhanced turbulence and a uniform northerly wind direction at all observation levels of the 10-m mast. Also the gradient and bulk Richardson numbers drop to values between 0 and 0.25. The following period is characterized by weak but increasing stability with continuous turbulence. Some weaker wave activity remains clearly visible in our observations.

Although the origin of the process leading to the shift in wind direction near the surface and the resulting enhanced directional wind shear remains unclear, this case nicely illustrates the importance of local wind shear for triggering the instability of near-surface wave.

IOP-10/III, TURBULENCE INTENSIFICATION THROUGH WAVE BREAKING. The LATAN-3M sodar recorded a very clear and strong harmonic signal starting at 0010 UTC (Fig. 10f) between 100 m and 200 m, which resulted in a major instability at 0037 UTC. Near the surface, the turbulence was enhanced substantially, as observed by the EC systems at 2.0, 4.5, and 10.3 m (Figs. 10d,e). The harmonic oscillations with a period of about 4 min can also be observed in the horizontal and vertical velocity components (Figs. 10b,d) of the WCv1 and the 10-m mast. The oscillations in horizontal and vertical velocity are 180° out of phase, consistent with internal gravity waves (Sun et al. 2015).

The preceding period is at first characterized by a strong, surface-based inversion (Fig. 10a) topping out at about 100 m with light, meandering winds roughly from southeast (Figs. 10b,c), occasionally showing the signature of wind veer resembling an Ekman spiral (e.g., as seen around 2310 UTC). The turbulence detected by the three sonic anemometers is very weak and of intermittent character. Between 2340 and 2350 UTC the wind direction shifts to a rather northerly direction at all levels below 200 m (see also Fig. 7d) and the wind speeds drop. The upper level winds, at heights between 46 and 85 m, accelerate gently until the wave breaks at 0037 UTC.

For an in-depth analysis, the UAS temperature and lidar wind speed profiles sampled at 2342, 0009, and 0030 UTC (mean UAS flight time) offer further insight in the dynamics of this event (Fig. 11a). These profiles indicate some cooling above 50 m, whereas wind speeds increase below 75 m and decrease above this level, resulting in the formation of a LLJ as seen in the last profile. This corresponds to strong downward transport of momentum as seen in the time height diagram for wind speed (Fig. 11c). Estimates of Ri for the three profiles (Fig. 11b) indicate the formation of a dynamically weakly stable layer (Ri < 0.25) right below 150 m, between the time of the first and second profile, which then propagates downward. This locally weakly stable layer is largely related to the sharp wind speed gradients above the LLJ core. Just about 7 min after the last UAS profile, the wave breaks and strongly enhances

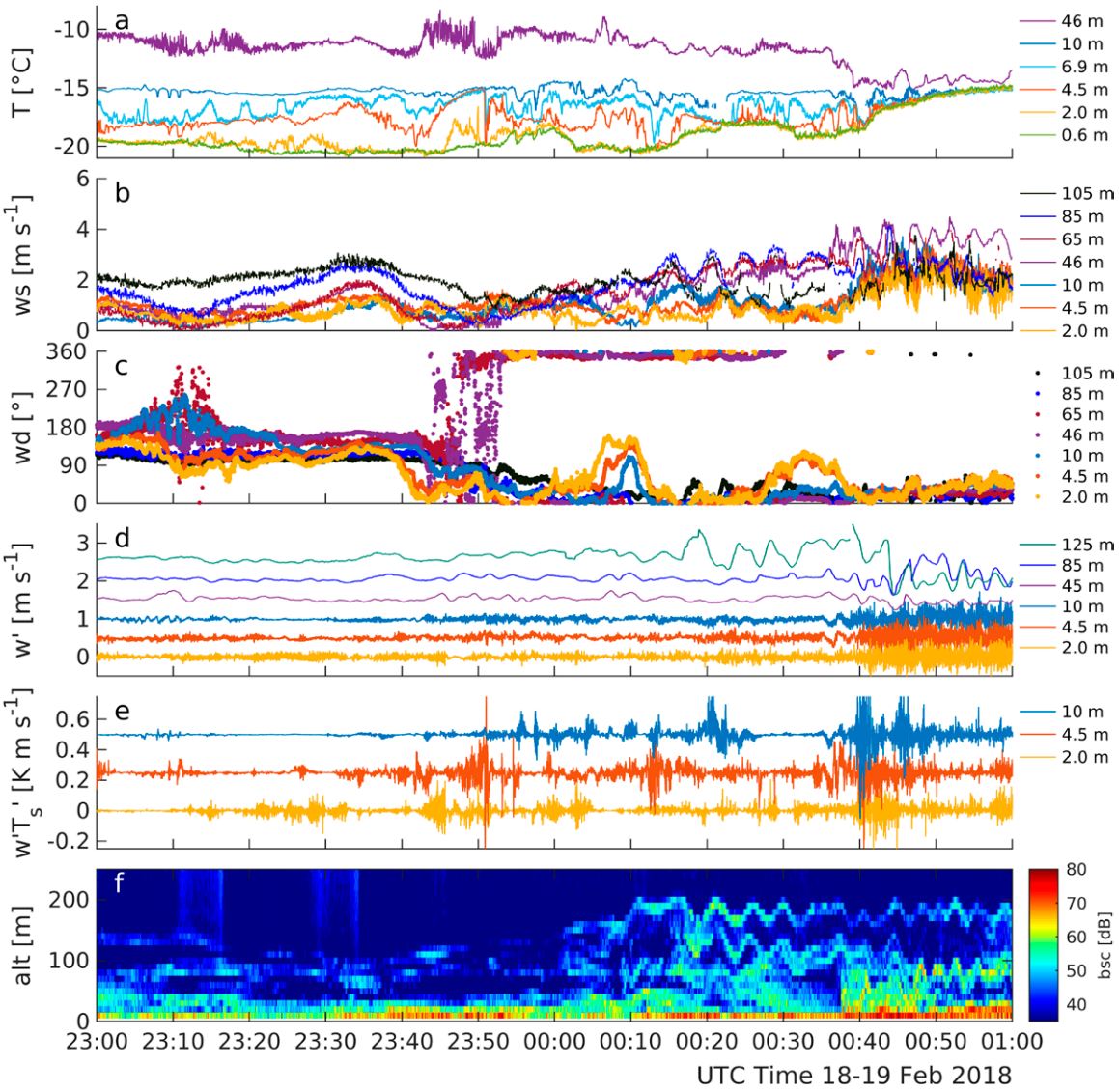

Fig. 10. Time series of various atmospheric parameters during IOP-10, 2300 UTC 18 Feb–0100 UTC 19 Feb 2018: (a) temperature (observed by GFI2 and FMI); (b) wind speed (GFI2, FMI, and WCv1); (c) wind direction (GFI2, FMI, and WCv1); (d) vertical velocity (GFI2, WCv1); (e) instantaneous kinematic heat flux (GFI2); (f) sodar attenuated backscatter profiles (LATAN-3M). The vertical velocity and kinematic heat flux data are shifted by increments of 0.5 m s^{-1} and 0.25 K m s^{-1} respectively, to reveal structures.

the turbulence near the surface. The wavelet spectral energy estimate of the vertical wind component observed at 10 m (Fig. 11d) indicates very weak turbulence before 0037 UTC. The wave-breaking event is characterized by a very strong signal with a period of about 3 min, which triggers a turbulence cascade to smaller scales. After 0100 UTC, the strong 3-min signal begins to vanish and the small-scale turbulence weakens again.

The wave breaking event ends at 0050 UTC and after this the wave appears to have higher frequency (Fig. 10f). This is most likely due to the Doppler shift caused by the increasing wind speeds at the levels above 125 m (Fig. 11c).

Summary and outlook

ISOBAR is an experimental research project targeting the SBL over Arctic sea ice by means of a novel observational approach based on a combination of ground-based in situ and remote sensing instrumentation with multiple unmanned aircraft systems. Two major field campaigns, ISOBAR17 and ISOBAR18, were carried out at the Finnish island Hailuoto in the

ice-covered Bothnian Bay, each lasting for about one month in February 2017 and 2018. These campaigns were characterized by contrasting conditions, with little sea ice and relatively mild temperatures in 2017, whereas conditions were closer to the climatological mean in 2018, favoring more frequent VSBL formation. With our observation strategy of extensive UAS-based measurements supplemented by surface-based mast and remote sensing observations, we have sampled comprehensive SBL datasets, including 14 IOPs; these datasets offer unprecedented spatiotemporal resolution, while also displaying good agreement between the different systems.

Frequent UAS profiles allow for detailed insight into the evolution of the SBL, which may be subject to rapid temperature changes affecting the entire ABL, and small-scale thermal instabilities within the otherwise stably stratified ABL. These data also allow for detailed studies on various VSBL processes and their interaction with near-surface turbulence, of which we highlight three examples, all observed during the same IOP: first, a shear instability caused by the lowering and intensification of the LLJ; second, an unusual rapid-cooling event at elevated levels around 10 m, which appears to be caused by the interaction of a near-surface wave with local shear and the modulation of the surface-layer static stability associated with this nonlinear wave; third, a wave instability related to the intensification of shear at the top of a forming LLJ, triggering enhanced turbulence near the surface. The nature and interactions of such VSBL processes, as well as the potential deviations from similarity theory associated with them, will be subject to more systematic studies also making use of other SBL datasets such as SHEBA (Grachev et al. 2008) or CASES-99 (Poulos et al. 2002).

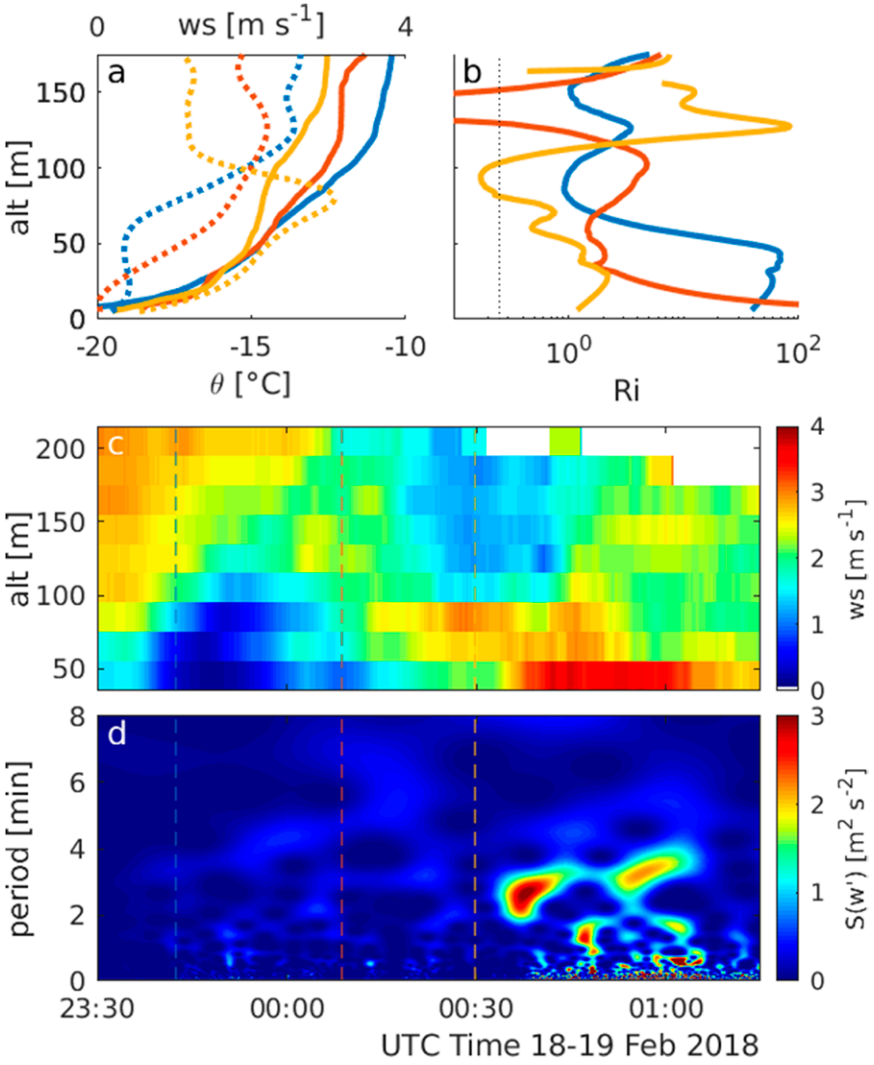

Fig. 11. Observations of (a) UAS profiles of potential temperature and corresponding lidar wind speed profiles; (b) resulting profiles of Ri; (c) time–height diagram of lidar wind speed; and (d) wavelet energy of 10-m sonic vertical velocity component during IOP-10, 2330 UTC 18 Feb–0130 UTC 19 Feb 2018. The black dotted line in (b) indicates Ri = 0.25. The UAS flight times from (a) and (b) are indicated as vertical lines in the same color in (c) and (d).

Furthermore, the ISOBAR datasets provide an excellent opportunity to study the transition from WSBL to VSBL, which is important for a better understanding of the conditions leading to strong surface-based temperature inversions and associated extremely cold temperatures. In particular, we aim to investigate the relative importance of local and large-scale conditions. In a follow-up project, we aim to identify and classify the various mechanisms behind the

SBL model simulations

To illustrate current challenges in SBL modeling, three different types of numerical models were used to simulate the SBL evolution during IOP-14 (23–24 February 2018): the MetCoOp Ensemble Prediction System (MEPS), the Weather Research and Forecasting Model in its single-column mode (WRF-SCM), and the Parallelized Large-Eddy Simulation Model (PALM). MEPS (Müller et al. 2017) is an operational NWP system covering the Nordic countries, forced at its boundaries by the global ECMWF-IFS (Bauer et al. 2013). There are 65 vertical model levels, with the first level at 12.5 m AGL and decreasing vertical resolution aloft. Surface–atmosphere and surface–soil processes are described by the Surface Externaliseé (SURFEX) model (Masson et al. 2013). WRF-SCM utilizes the full WRF physics (Skamarock et al. 2008), with Mellor–Yamada–Nakanishi–Niino turbulence parameterization (Nakanishi and Niino 2006), within an atmospheric column with 200 vertical levels. The vertical spacing is about 2 m in the lower atmosphere. Hourly geostrophic winds and advection of momentum, temperature and humidity are derived from a mesoscale WRF simulation (Sterk et al. 2015). PALM (Maronga et al. 2015, 2020) runs at a grid spacing of 2 m and a model domain of 500^3 m^3 using a standard configuration but with a modified Deardorff subgrid-scale closure as described by Dai et al. (2021) and coupled to the Rapid Radiative Transfer Model (Clough et al. 2005). PALM is initialized by the same vertical profiles as WRF-SCM and forced by skin temperatures observed during IOP-14.

Figure SB1 shows that even though all three models are capable of forming a very stable stratification and cold air at the surface, the model results differ considerably. The formation of cold air above the surface and the associated strong vertical (temperature) gradients are best captured by PALM, while both MEPS and WRF-SCM display a deeper SBL with weaker gradients. At heights between 50 and 300 m, both WRF-SCM and PALM produce weaker temperature gradients, which can be ascribed to deficiencies in the model initialization. MEPS here captures the stratification much better. Overall, the three different models show substantial deviations from the observations in the lower atmosphere.

Likely sources for these deviations are the turbulence parameterizations that overestimate turbulent mixing and the associated downward heat flux from the atmosphere to the cold surface, and the different boundary conditions and initial conditions applied. As PALM resolves most of the turbulent transport, it can more adequately represent the SBL evolution close to the surface. It is noteworthy that PALM and WRF-SCM, despite being initialized with the same profiles, produce quite different SBLs. Research models like WRF-SCM and PALM are highly sensitive to the initial profiles and boundary conditions, which are either derived from measurements or larger-scale model data and thus come with an inherent uncertainty. All three models depend on accurate surface properties, for which a combination of measurements and ad hoc estimations was used here. The differences present in these simulations epitomize the necessity for deeper understanding of the SBL and its representation in atmospheric models; an understanding that is expedited by unique, finescale observational datasets, such as ISOBAR. Sensitivities to model physics and surface properties during IOP-14 are subject of an ongoing study, following the process-based analysis by Sterk et al. (2016).

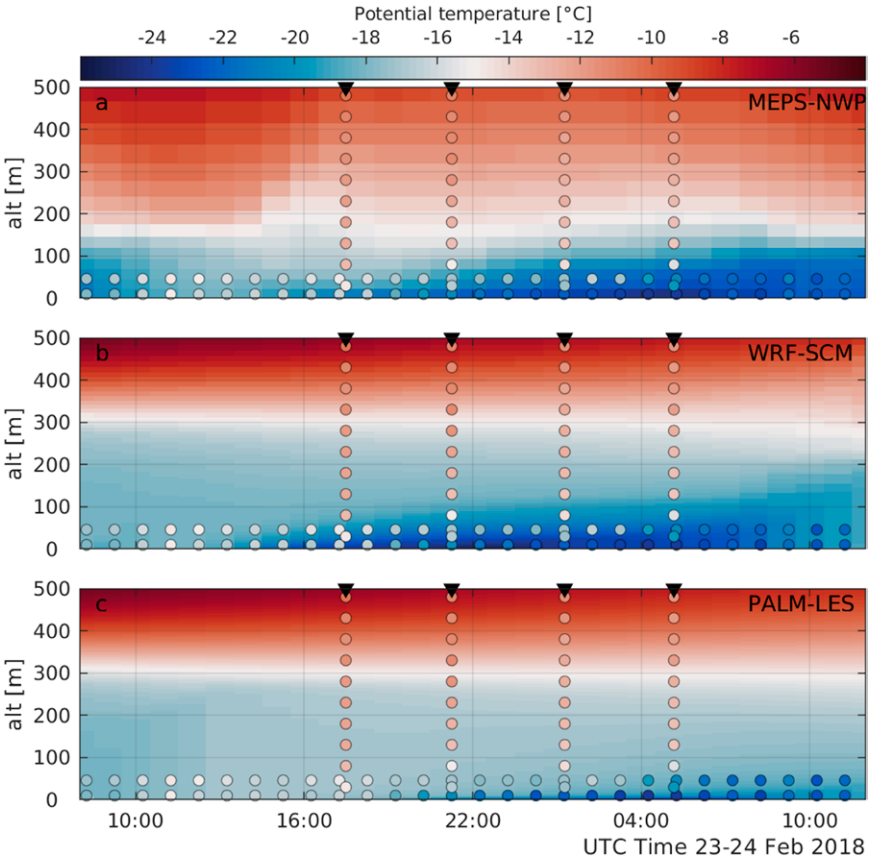

Fig. SB1. Time–height plots of potential temperature from the MEPS forecast (MEPS-NWP), the WRF single-column simulation (WRF-SCM), and the PALM LES simulation (PALM-LES). The data cover the lowermost 500 m and the first 24 h at the measurement site. Observations from SUMO, GFI, and FMI are superimposed as circles.

generation of intermittency in the VSBL, based on the ISOBAR and other datasets. This classification should form the basis for a stochastic parameterization for intermittent turbulence in mesoscale NWP models. Additionally, the UAS profiles gathered during ISOBAR—with such unique spatiotemporal resolution—offer a new perspective for SBL studies by applying an alternative gradient-based scaling scheme (Sorbjan 2010). The application of this method allows the determination of vertical profiles of turbulent parameters, which could aid the development of new NWP parameterizations.

Initial numerical modeling experiments have confirmed that the structure of the VSBL is inadequately represented in state-of-the-art NWP and SCM. A complementary large-eddy simulation (LES) experiment showed that turbulence-resolving simulations are able to reproduce even very shallow stable layers and thus provide a powerful tool for studying turbulent processes in such conditions. In a next step we thus plan to perform an LES study to evaluate the gradient-based similarity relationships. In this way, we hope to develop a turbulence parameterization, to be implemented in both NWP and SCM models and finally to be evaluated against measurement data obtained during the IOP periods. Moreover, we strive to analyze LES data with respect to phenomena observed during the IOPs and to perform virtual flights in the LES model to evaluate and improve flight strategies for future UAS campaigns.

Acknowledgments. We would like to acknowledge all campaign participants (see Table 1) for their dedication and enthusiasm that largely contributed to the success of the two field campaigns in often challenging conditions. A special thanks from all participants is dedicated to our local hosts at Hailuodon Majakkapiha, Hannu Korpela, Sanna Ahomäki, and Pekka Tervonen. Hannu and Sanna were just amazing in perfectly organizing all required logistics and solving all the large and small challenges and problems certainly occurring during extensive field work. And our campaign chef Pekka was spoiling us with superb meals, an important factor for a successful campaign that never should be underestimated. Furthermore, we thank Anak Bhandari for his efforts and commitment in the preparation of the instrumentation upfront the campaign, the organization of the transport, and the cleanup after return. We would also like to thank Priit Tisler from FMI for his advice on UAS operations in Finland and for connecting us with the right persons and organizations. With respect to the flight permission process we are very grateful to the Finnish aviation authority TRAFI for their very positive attitude, competent guidance, and a fast and nonbureaucratic handling of our applications. We also highly appreciate the uncomplicated communication with the Air Traffic Control (ATC) at Oulu airport that allowed us to focus on science when operating UAS.

The ISOBAR project was funded by the Research Council of Norway (RCN) under the FRINATEK scheme (Project 251042/F20). The scanning wind lidar system (WC100S), used during ISOBAR17 and the WCv1 lidar wind profiler and the MFAS sodar used during ISOBAR18, have been made available via the National Norwegian infrastructure project OBLO (Offshore Boundary Layer Observatory) also funded by RCN (Project 227777). The work of GHU, TV, and IS was also supported by the Academy of Finland (Contract 304345). Financial support was also provided in part by the National Science Foundation under Grant 1539070 and internal funding from the University of Oklahoma. The WRF-SCM simulations were performed on resources provided by UNINETT Sigma2—the National Infrastructure for High Performance Computing and Data Storage in Norway. Finally we would like to express our gratitude to our esteemed colleague Zbigniev Sorbjan, who unfortunately passed away by far too early in February 2017, just during the first ISOBAR campaign.

Appendix: List of abbreviations

Table A1 provides a list of abbreviations that appear in the paper along with their expansions.

Table A1. Abbreviations and expansions.

AMOR Q13	Advanced Mission and Operation Research Quadcopter (13-in propellers)
B2M	Bebop2Met
CS	CopterSonde
EC	Eddy covariance
ECMWF-IFS	ECMWF Integrated Forecasting System
FMI	Finnish Meteorological Institute
GFI	Geophysical Institute, University of Bergen
ISOBAR	Innovative Strategies for Observations in the Arctic Atmospheric Boundary Layer
Lidar	Light detection and ranging
LLJ	Low-level jet
MASC	Multi-Purpose Airborne Sensor Carrier
MEPS	MetCoOp Ensemble Prediction System
MFAS	Medium size flat array sodar
MOST	Monin–Obukhov similarity theory
OU	University of Oklahoma
QA/QC	Quality assurance and quality check
RRTMG	Rapid Radiative Transfer Model Global
SBL	Stable boundary layer
SCM	Single-column model
Sodar	Sound detection and ranging
SUMO	Small Meteorological Observer
UAS	Unmanned aircraft system
UOWL	Ostwestfalen-Lippe UASA
UT	University of Tübingen
VSBL	Very stable boundary layer
WCv1	Windcube v1
WC100S	Windcube 100S
WSBL	Weakly stable boundary layer

References

Atlaskin, E., and T. Vihma, 2012: Evaluation of NWP results for wintertime nocturnal boundary-layer temperatures over Europe and Finland. *Quart. J. Roy. Meteor. Soc.*, **138**, 1440–1451, https://doi.org/10.1002/qj.1885.

Bauer, P., and Coauthors, 2013: Model cycle 38r2: Components and performance. ECMWF Tech. Memo 704, 60 pp., https://doi.org/10.21957/XC1R0LJ6l.

Beare, R. J., 2007: Boundary layer mechanisms in extratropical cyclones. *Quart. J. Roy. Meteor. Soc.*, **133**, 503–515, https://doi.org/10.1002/qj.30.

Bell, T. M., B. R. Greene, P. M. Klein, M. Carney, and P. B. Chilson, 2020: Confronting the boundary layer data gap: Evaluating new and existing methodologies of probing the lower atmosphere. *Atmos. Meas. Tech.*, **13**, 3855–3872, https://doi.org/10.5194/amt-13-3855-2020.

Bintanja, R., E. C. van der Linden, and W. Hazeleger, 2012: Boundary layer stability and Arctic climate change: A feedback study using EC-Earth. *Climate Dyn.*, **39**, 2659–2673, https://doi.org/10.1007/s00382-011-1272-1.

Bonin, T., P. Chilson, B. Zielke, and E. Fedorovich, 2013: Observations of the early evening boundary-layer transition using a small unmanned aerial system. *Bound.-Layer Meteor.*, **146**, 119–132, https://doi.org/10.1007/s10546-012-9760-3.

Bosveld, F. C., and Coauthors, 2014: The third GABLS intercomparison case for evaluation studies of boundary-layer models. Part B: Results and process understanding. *Bound.-Layer Meteor.*, **152**, 157–187, https://doi.org/10.1007/s10546-014-9919-1.

Byrkjedal, Ø., I. Esau, and N. G. Kvamstø, 2007: Sensitivity of simulated wintertime Arctic atmosphere to vertical resolution in the ARPEGE/IFS model. *Climate Dyn.*, **30**, 687–701, https://doi.org/10.1007/s00382-007-0316-z.

Cassano, J. J., 2013: Observations of atmospheric boundary layer temperature profiles with a small unmanned aerial vehicle. *Antarct. Sci.*, **26**, 205–213, https://doi.org/10.1017/S0954102013000539.

——, J. A. Maslanik, C. J. Zappa, A. L. Gordon, R. I. Cullather, and S. L. Knuth, 2010: Observations of Antarctic polynya with unmanned aircraft systems. *Eos, Trans. Amer. Geophys. Union*, **91**, 245, https://doi.org/10.1029/2010EO280001.

Chilson, P. B., and Coauthors, 2009: SMARTSonde: A small UAS platform to support radar research. *Proc. 34th Conf. on Radar Meteorology*, Norman, OK, Amer. Meteor. Soc., 12B.6, https://ams.confex.com/ams/34Radar/techprogram/paper_156396.htm.

Clough, S. A., M. W. Shephard, E. J. Mlawer, J. S. Delamere, M. J. Iacono, K. Cady-Pereira, S. Boukabara, and P. D. Brown, 2005: Atmospheric radiative transfer modeling: A summary of the AER codes. *J. Quant. Spectrosc. Radiat. Transfer*, **91**, 233–244, https://doi.org/10.1016/j.jqsrt.2004.05.058.

Curry, J. A., J. Maslanik, G. Holland, and J. Pinto, 2004: Applications of aerosondes in the Arctic. *Bull. Amer. Meteor. Soc.*, **85**, 1855–1862, https://doi.org/10.1175/BAMS-85-12-1855.

Cuxart, J., and Coauthors, 2000: Stable Atmospheric Boundary-Layer Experiment in Spain (SABLES 98): A report. *Bound.-Layer Meteor.*, **96**, 337–370, https://doi.org/10.1023/A:1002609509707.

——, and Coauthors, 2005: Single-column model intercomparison for a stably stratified atmospheric boundary layer. *Bound.-Layer Meteor.*, **118**, 273–303, https://doi.org/10.1007/s10546-005-3780-1.

——, and Coauthors, 2016: Estimation of the advection effects induced by surface heterogeneities in the surface energy budget. *Atmos. Chem. Phys.*, **16**, 9489–9504, https://doi.org/10.5194/acp-16-9489-2016.

Dai, A., D. Luo, M. Song, and J. Liu, 2019: Arctic amplification is caused by sea-ice loss under increasing CO_2. *Nat. Commun.*, **10**, 121, https://doi.org/10.1038/s41467-018-07954-9.

Dai, Y., S. Basu, B. Maronga, and S. R. de Roode, 2021: Addressing the grid-size sensitivity issue in large-eddy simulations of stable boundary layers. *Bound.-Layer Meteor.*, **178**, 63–89, https://doi.org/10.1007/s10546-020-00558-1.

Davy, R., and I. Esau, 2016: Differences in the efficacy of climate forcings explained by variations in atmospheric boundary layer depth. *Nat. Commun.*, **7**, 11690, https://doi.org/10.1038/ncomms11690.

de Boer, G., and Coauthors, 2015: The Pilatus unmanned aircraft system for lower atmospheric research. *Atmos. Meas. Tech.*, **9**, 1845–1857, https://doi.org/10.5194/amt-9-1845-2016.

——, and Coauthors, 2018: A bird's-eye view: Development of an operational ARM unmanned aerial capability for atmospheric research in Arctic Alaska. *Bull. Amer. Meteor. Soc.*, **99**, 1197–1212, https://doi.org/10.1175/BAMS-D-17-0156.1.

——, and Coauthors, 2019: Development of community, capabilities and understanding through unmanned aircraft-based atmospheric research: The LAPSE-RATE campaign. *Bull. Amer. Meteor. Soc.*, **101**, E684–E699, https://doi.org/10.1175/BAMS-D-19-0050.1.

Egger, J., and Coauthors, 2002: Diurnal winds in the Himalayan Kali Gandaki valley. Part III: Remotely piloted aircraft soundings. *Mon. Wea. Rev.*, **130**, 2042–2058, https://doi.org/10.1175/1520-0493(2002)130<2042:DWITHK>2.0.CO;2.

——, and Coauthors, 2005: Diurnal circulation of the Bolivian Altiplano. Part I: Observations. *Mon. Wea. Rev.*, **133**, 911–924, https://doi.org/10.1175/MWR2894.1.

Elston, J., B. Argrow, M. Stachura, D. Weibel, D. Lawrence, and D. Pope, 2015: Overview of small fixed-wing unmanned aircraft for meteorological sampling. *J. Atmos. Oceanic Technol.*, **32**, 97–115, https://doi.org/10.1175/JTECH-D-13-00236.1.

Fernando, H. J. S., and J. C. Weil, 2010: Whither the stable boundary layer? *Bull. Amer. Meteor. Soc.*, **91**, 1475–1484, https://doi.org/10.1175/2010BAMS2770.1.

——, and Coauthors, 2015: The MATERHORN: Unraveling the intricacies of mountain weather. *Bull. Amer. Meteor. Soc.*, **96**, 1945–1967, https://doi.org/10.1175/BAMS-D-13-00131.1.

Foken, T., 2006: 50 years of the Monin–Obukhov similarity theory. *Bound.-Layer Meteor.*, **119**, 431–447, https://doi.org/10.1007/s10546-006-9048-6.

Gentine, P., G.-J. Steeneveld, B. G. Heusinkveld, and A. A. Holtslag, 2018: Coupling between radiative flux divergence and turbulence near the surface. *Quart. J. Roy. Meteor. Soc.*, **144**, 2491–2507, https://doi.org/10.1002/qj.3333.

Goger, B., M. W. Rotach, A. Gohm, O. Fuhrer, I. Stiperski, and A. A. M. Holtslag, 2018: The impact of three-dimensional effects on the simulation of turbulence kinetic energy in a major Alpine valley. *Bound.-Layer Meteor.*, **168**, 1–27, https://doi.org/10.1007/s10546-018-0341-y.

Grachev, A. A., E. L. Andreas, C. W. Fairall, P. S. Guest, and P. O. G. Persson, 2008: Turbulent measurements in the stable atmospheric boundary layer during SHEBA: Ten years after. *Acta Geophys.*, **56**, 142–166, https://doi.org/10.2478/s11600-007-0048-9.

——, ——, ——, ——, and ——, 2013: The critical Richardson number and limits of applicability of local similarity theory in the stable boundary layer. *Bound.-Layer Meteor.*, **147**, 51–82, https://doi.org/10.1007/s10546-012-9771-0.

Graham, R. M., and Coauthors, 2019: Evaluation of six atmospheric reanalyses over Arctic sea ice from winter to early summer. *J. Climate*, **32**, 4121–4143, https://doi.org/10.1175/JCLI-D-18-0643.1.

Greene, B., A. Segales, T. Bell, E. Pillar-Little, and P. Chilson, 2019: Environmental and sensor integration influences on temperature measurements by rotary-wing unmanned aircraft systems. *Sensors*, **19**, 1470, https://doi.org/10.3390/s19061470.

Heppelmann, T., A. Steiner, and S. Vogt, 2017: Application of numerical weather prediction in wind power forecasting: Assessment of the diurnal cycle. *Meteor. Z.*, **26**, 319–331, https://doi.org/10.1127/metz/2017/0820.

Hersbach, H., and Coauthors, 2020: The ERA5 global reanalysis. *Quart. J. Roy. Meteor. Soc.*, **146**, 1999–2049, https://doi.org/10.1002/qj.3803.

Hoch, S. W., P. Calanca, R. Philipona, and A. Ohmura, 2007: Year-round observation of longwave radiative flux divergence in Greenland. *J. Appl. Meteor. Climatol.*, **46**, 1469–1479, https://doi.org/10.1175/JAM2542.1.

Holland, G. J., and Coauthors, 2001: The aerosonde robotic aircraft: A new paradigm for environmental observations. *Bull. Amer. Meteor. Soc.*, **82**, 889–901, https://doi.org/10.1175/1520-0477(2001)082<0889:TARAAN>2.3.CO;2.

Holtslag, A., and Coauthors, 2013: Stable atmospheric boundary layers and diurnal cycles: Challenges for weather and climate models. *Bull. Amer. Meteor. Soc.*, **94**, 1691–1706, https://doi.org/10.1175/BAMS-D-11-00187.1.

Houston, A. L., B. Argrow, J. Elston, J. Lahowetz, E. W. Frew, and P. C. Kennedy, 2012: The Collaborative Colorado–Nebraska Unmanned Aircraft System Experiment. *Bull. Amer. Meteor. Soc.*, **93**, 39–54, https://doi.org/10.1175/2011BAMS3073.1.

Jakobson, E., T. Vihma, T. Palo, L. Jakobson, H. Keernik, and J. Jaagus, 2012: Validation of atmospheric reanalyses over the central Arctic Ocean. *Geophys. Res. Lett.*, **39**, L10802, https://doi.org/10.1029/2012GL051591.

Jonassen, M. O., H. Ólafsson, H. Ágústsson, O. Rögnvaldsson, and J. Reuder, 2012: Improving high-resolution numerical weather simulations by assimilating data from an unmanned aerial system. *Mon. Wea. Rev.*, **140**, 3734–3756, https://doi.org/10.1175/MWR-D-11-00344.1.

——, P. Tisler, B. Altstädter, A. Scholtz, T. Vihma, A. Lampert, G. König-Langlo, and C. Lüpkes, 2015: Application of remotely piloted aircraft systems in observing the atmospheric boundary layer over Antarctic sea ice in winter. *Polar Res.*, **34**, 25651, https://doi.org/10.3402/POLAR.V34.25651.

——, I. Välisuo, T. Vihma, P. Uotila, A. P. Makshtas, and J. Launiainen, 2019: Assessment of atmospheric reanalyses with independent observations in the Weddell Sea, the Antarctic. *J. Geophys. Res. Atmos.*, **124**, 12 468–12 484, https://doi.org/10.1029/2019JD030897.

Karsisto, V., S. Tijm, and P. Nurmi, 2017: Comparing the performance of two road weather models in the Netherlands. *Wea. Forecasting*, **32**, 991–1006, https://doi.org/10.1175/WAF-D-16-0158.1.

Knuth, S. L., and J. J. Cassano, 2014: Estimating sensible and latent heat fluxes using the integral method from in situ aircraft measurements. *J. Atmos. Oceanic Technol.*, **31**, 1964–1981, https://doi.org/10.1175/JTECH-D-14-00008.1.

Konrad, T. G., M. L. Hill, J. R. Rowland, and J. H. Meyer, 1970: A small, radio-controlled aircraft as a platform for meteorological sensor. *APL Tech. Dig.*, **10**, 11–19.

Kouznetsov, R. D., 2009: The multi-frequency sodar with high temporal resolution. *Meteor. Z.*, **18**, 169–173, https://doi.org/10.1127/0941-2948/2009/0373.

Kral, S., and Coauthors, 2018: Innovative Strategies for Observations in the Arctic Atmospheric Boundary Layer (ISOBAR)—The Hailuoto 2017 campaign. *Atmosphere*, **9**, 268, https://doi.org/10.3390/atmos9070268.

Kumer, V.-M., J. Reuder, and B. R. Furevik, 2014: A comparison of lidar and radiosonde wind measurements. *Energy Procedia*, **53**, 214–220, https://doi.org/10.1016/j.egypro.2014.07.230.

——, ——, M. Dorninger, R. Zauner, and V. Grubišić, 2016: Turbulent kinetic energy estimates from profiling wind lidar measurements and their potential for wind energy applications. *Renewable Energy*, **99**, 898–910, https://doi.org/10.1016/j.renene.2016.07.014.

Langford, J. S., and K. A. Emanuel, 1993: An unmanned aircraft for dropwindsonde deployment and hurricane reconnaissance. *Bull. Amer. Meteor. Soc.*, **74**, 367–375, https://doi.org/10.1175/1520-0477(1993)074<0367:AUAFDD>2.0.CO;2.

Lapworth, A., and S. R. Osborne, 2019: Gravity-wave drag in the stable boundary layer over moderate terrain. *Bound.-Layer Meteor.*, **171**, 175–189, https://doi.org/10.1007/s10546-018-00422-3.

Lesins, G., T. J. Duck, and J. R. Drummond, 2012: Surface energy balance framework for Arctic amplification of climate change. *J. Climate*, **25**, 8277–8288, https://doi.org/10.1175/JCLI-D-11-00711.1.

Lothon, M., and Coauthors, 2014: The BLLAST field experiment: Boundary-Layer Late Afternoon and Sunset Turbulence. *Atmos. Chem. Phys.*, **14**, 10 931–10 960, https://doi.org/10.5194/acp-14-10931-2014.

Louis, J.-F., 1979: A parametric model of vertical eddy fluxes in the atmosphere. *Bound.-Layer Meteor.*, **17**, 187–202, https://doi.org/10.1007/BF00117978.

Mahrt, L., 2003: Stably stratified boundary layer. *Encyclopedia of Atmospheric Sciences*, Elsevier, 298–305.

——, 2011: The near-calm stable boundary layer. *Bound.-Layer Meteor.*, **140**, 343–360, https://doi.org/10.1007/s10546-011-9616-2.

——, 2014: Stably stratified atmospheric boundary layers. *Annu. Rev. Fluid Mech.*, **46**, 23–45, https://doi.org/10.1146/annurev-fluid-010313-141354.

Maronga, B., and Coauthors, 2015: The Parallelized Large-Eddy Simulation Model (PALM) version 4.0 for atmospheric and oceanic flows: Model formulation, recent developments, and future perspectives. *Geosci. Model Dev.*, **8**, 2515–2551, https://doi.org/10.5194/gmd-8-2515-2015.

——, and Coauthors, 2020: Overview of the PALM model system 6.0. *Geosci. Model Dev.*, **13**, 1335–1372, https://doi.org/10.5194/gmd-13-1335-2020.

Martínez, D., M. A. Jiménez, J. Cuxart, and L. Mahrt, 2010: Heterogeneous nocturnal cooling in a large basin under very stable conditions. *Bound.-Layer Meteor.*, **137**, 97–113, https://doi.org/10.1007/s10546-010-9522-z.

Masson, V., and Coauthors, 2013: The SURFEXv7.2 land and ocean surface platform for coupled or offline simulation of Earth surface variables and fluxes. *Geosci. Model Dev.*, **6**, 929–960, https://doi.org/10.5194/gmd-6-929-2013.

Mayer, S., G. Hattenberger, P. Brisset, M. Jonassen, and J. Reuder, 2012a: A 'no-flow-sensor' wind estimation algorithm for unmanned aerial systems. *Int. J. Micro Air Veh.*, **4**, 15–30, https://doi.org/10.1260/1756-8293.4.1.15.

——, M. Jonassen, A. Sandvik, and J. Reuder, 2012b: Profiling the Arctic stable boundary layer in Advent valley, Svalbard: Measurements and simulations. *Bound.-Layer Meteor.*, **143**, 507–526, https://doi.org/10.1007/s10546-012-9709-6.

——, A. Sandvik, M. Jonassen, and J. Reuder, 2012c: Atmospheric profiling with the UAS SUMO: A new perspective for the evaluation of fine-scale atmospheric models. *Meteor. Atmos. Phys.*, **116**, 15–26, https://doi.org/10.1007/s00703-010-0063-2.

McNider, R. T., J. R. Christy, and A. Biazar, 2010: A stable boundary layer perspective on global temperature trends. *IOP Conf. Ser.: Earth Environ. Sci.*, **231**, 012003, https://doi.org/10.1088/1755-1315/13/1/012003.

Monin, A. S., and A. M. Obukhov, 1954: Basic laws of turbulent mixing in the atmosphere near the ground. *Tr. Geofiz. Inst., Akad. Nauk SSSR*, **24**, 163–187.

Müller, M., and Coauthors, 2017: AROME-MetCoOp: A Nordic convective-scale operational weather prediction model. *Wea. Forecasting*, **32**, 609–627, https://doi.org/10.1175/WAF-D-16-0099.1.

Nakanishi, M., and H. Niino, 2006: An improved Mellor–Yamada level-3 model: Its numerical stability and application to a regional prediction of advection fog. *Bound.-Layer Meteor.*, **119**, 397–407, https://doi.org/10.1007/s10546-005-9030-8.

Nappo, C., 2012: *An Introduction to Atmospheric Gravity Waves*. Academic Press, 400 pp.

Neumann, P. P., and M. Bartholmai, 2015: Real-time wind estimation on a micro unmanned aerial vehicle using its inertial measurement unit. *Sens. Actuators A Phys.*, **235**, 300–310, https://doi.org/10.1016/j.sna.2015.09.036.

Nieuwstadt, F. T. M., 1984: The turbulent structure of the stable, nocturnal boundary layer. *J. Atmos. Sci.*, **41**, 2202–2216, https://doi.org/10.1175/1520-0469(1984)041<2202:TTSOTS>2.0.CO;2.

——, 1985: A model for the stationary, stable boundary layer. *Turbulence and Diffusion in Stable Environments*, J. C. R. Hunt, Ed., Clarendon Press, 149–179.

Palomaki, R. T., N. T. Rose, M. van den Bossche, T. J. Sherman, and S. F. J. D. Wekker, 2017: Wind estimation in the lower atmosphere using multirotor aircraft. *J. Atmos. Oceanic Technol.*, **34**, 1183–1191, https://doi.org/10.1175/JTECH-D-16-0177.1.

Persson, P. O. G., C. W. Fairall, E. L. Andreas, P. G. Guest, and D. K. Perovich, 2002: Measurements near the atmospheric surface flux group tower at SHEBA: Near-surface conditions and surface energy budget. *J. Geophys. Res.*, **107**, 8045, https://doi.org/10.1029/2000JC000705.

Pithan, F., and T. Mauritsen, 2014: Arctic amplification dominated by temperature feedbacks in contemporary climate models. *Nat. Geosci.*, **7**, 181–184, https://doi.org/10.1038/ngeo2071.

Poulos, G. S., and Coauthors, 2002: CASES-99: A comprehensive investigation of the stable nocturnal boundary layer. *Bull. Amer. Meteor. Soc.*, **83**, 555–581, https://doi.org/10.1175/1520-0477(2002)083<0555:CACIOT>2.3.CO;2.

Rautenberg, A., and Coauthors, 2019: The multi-purpose airborne sensor carrier MASC-3 for wind and turbulence measurements in the atmospheric boundary layer. *Sensors*, **19**, 2292, https://doi.org/10.3390/s19102292.

Reuder, J., P. Brisset, M. M. Jonassen, and S. Mayer, 2009: The Small Unmanned Meteorological Observer SUMO: A new tool for atmospheric boundary layer research. *Meteor. Z.*, **18**, 141–147, https://doi.org/10.1127/0941-2948/2009/0363.

——, M. O. Jonassen, and H. Ólafsson, 2012a: The Small Unmanned Meteorological Observer SUMO: Recent developments and applications of a micro-UAS for atmospheric boundary layer research. *Acta Geophys.*, **60**, 1454–1473, https://doi.org/10.2478/s11600-012-0042-8.

——, and Coauthors, 2012b: FLOHOF 2007: An overview of the mesoscale meteorological field campaign at Hofsjökull, central Iceland. *Meteor. Atmos. Phys.*, **116**, 1–13, https://doi.org/10.1007/s00703-010-0118-4.

——, L. Båserud, M. O. Jonassen, S. T. Kral, and M. Müller, 2016: Exploring the potential of the RPA system SUMO for multipurpose boundary-layer missions during the BLLAST campaign. *Atmos. Meas. Tech.*, **9**, 2675–2688, https://doi.org/10.5194/amt-9-2675-2016.

Román-Cascón, C., C. Yagüe, G.-J. Steeneveld, G. Morales, J. A. Arrillaga, M. Sastre, and G. Maqueda, 2019: Radiation and cloud-base lowering fog events: Observational analysis and evaluation of WRF and HARMONIE. *Atmos. Res.*, **229**, 190–207, https://doi.org/10.1016/j.atmosres.2019.06.018.

Segales, A. R., B. R. Greene, T. M. Bell, W. Doyle, J. J. Martin, E. A. Pillar-Little, and P. B. Chilson, 2020: The CopterSonde: An insight into the development of a smart unmanned aircraft system for atmospheric boundary layer research. *Atmos. Meas. Tech.*, **13**, 2833–2848, https://doi.org/10.5194/amt-13-2833-2020.

Serreze, M. C., and R. G. Barry, 2011: Processes and impacts of Arctic amplification: A research synthesis. *Global Planet. Change*, **77**, 85–96, https://doi.org/10.1016/j.gloplacha.2011.03.004.

——, A. P. Barrett, J. C. Stroeve, D. N. Kindig, and M. M. Holland, 2009: The emergence of surface-based Arctic amplification. *Cryosphere*, **3**, 11–19, https://doi.org/10.5194/tc-3-11-2009.

Skamarock, W., and Coauthors, 2008: A description of the Advanced Research WRF version 3. NCAR Tech. Note NCAR/TN-475+STR, 113 pp., https://doi.org/10.5065/D68S4MVH.

Sorbjan, Z., 2010: Gradient-based scales and similarity laws in the stable boundary layer. *Quart. J. Roy. Meteor. Soc.*, **136**, 1243–1254, https://doi.org/10.1002/qj.638.

——, and A. Grachev, 2010: An evaluation of the flux–gradient relationship in the stable boundary layer. *Bound.-Layer Meteor.*, **135**, 385–405, https://doi.org/10.1007/s10546-010-9482-3.

Spiess, T., J. Bange, M. Buschmann, and P. Vörsmann, 2007: First application of the meteorological Mini-UAV 'M2AV.' *Meteor. Z.*, **16**, 159–169, https://doi.org/10.1127/0941-2948/2007/0195.

Steeneveld, G. J., A. A. M. Holtslag, C. J. Nappo, B. J. H. van de Wiel, and L. Mahrt, 2008: Exploring the possible role of small-scale terrain drag on stable boundary layers over land. *J. Appl. Meteor. Climatol.*, **47**, 2518–2530, https://doi.org/10.1175/2008JAMC1816.1.

——, M. J. J. Wokke, C. D. G. Zwaaftink, S. Pijlman, B. G. Heusinkveld, A. F. G. Jacobs, and A. A. M. Holtslag, 2010: Observations of the radiation divergence in the surface layer and its implication for its parameterization in numerical weather prediction models. *J. Geophys. Res.*, **115**, D06107, https://doi.org/10.1029/2009JD013074.

Stephens, G. L., and Coauthors, 2000: The Department of Energy's Atmospheric Radiation Measurement (ARM) unmanned aerospace vehicle (UAV) program. *Bull. Amer. Meteor. Soc.*, **81**, 2915–2938, https://doi.org/10.1175/1520-0477(2000)081<2915:TDOESA>2.3.CO;2.

Sterk, H. A. M., G. J. Steeneveld, T. Vihma, P. S. Anderson, F. C. Bosveld, and A. A. M. Holtslag, 2015: Clear-sky stable boundary layers with low winds over snow-covered surfaces. Part I: WRF Model evaluation. *Quart. J. Roy. Meteor. Soc.*, **141**, 2165–2184, https://doi.org/10.1002/qj.2513.

——, ——, F. C. Bosveld, T. Vihma, P. S. Anderson, and A. A. M. Holtslag, 2016: Clear-sky stable boundary layers with low winds over snow-covered surfaces. Part II: Process sensitivity. *Quart. J. Roy. Meteor. Soc.*, **142**, 821–835, https://doi.org/10.1002/qj.2684.

Sun, J., and Coauthors, 2015: Review of wave–turbulence interactions in the stable atmospheric boundary layer. *Rev. Geophys.*, **53**, 956–993, https://doi.org/10.1002/2015RG000487.

Sun, Q. Z., T. Vihma, M. O. Jonassen, and Z. H. Zhang, 2020: Impact of assimilation of radiosonde and UAV-observations from the Southern Ocean in the polar WRF Model. *Adv. Atmos. Sci.*, **37**, 441–454, https://doi.org/10.1007/s00376-020-9213-8.

Svensson, G., and A. A. M. Holtslag, 2009: Analysis of model results for the turning of the wind and related momentum fluxes in the stable boundary layer. *Bound.-Layer Meteor.*, **132**, 261–277, https://doi.org/10.1007/s10546-009-9395-1.

Tjernström, M., and Coauthors, 2005: Modelling the Arctic boundary layer: An evaluation of six ARCMIP regional-scale models using data from the SHEBA project. *Bound.-Layer Meteor.*, **117**, 337–381, https://doi.org/10.1007/s10546-004-7954-z.

Uotila, P., T. Vihma, and J. Haapala, 2015: Atmospheric and oceanic conditions and the extremely low Bothnian Bay sea ice extent in 2014/2015. *Geophys. Res. Lett.*, **42**, 7740–7749, https://doi.org/10.1002/2015GL064901.

Uppala, S. M., and Coauthors, 2005: The ERA-40 Re-Analysis. *Quart. J. Roy. Meteor. Soc.*, **131**, 2961–3012, https://doi.org/10.1256/qj.04.176.

Uttal, T., and Coauthors, 2002: Surface heat budget of the Arctic Ocean. *Bull. Amer. Meteor. Soc.*, **83**, 255–275, https://doi.org/10.1175/1520-0477(2002)083<0255:SHBOTA>2.3.CO;2.

Van de Wiel, B. J. H., and Coauthors, 2017: Regime transitions in near-surface temperature inversions: A conceptual model. *J. Atmos. Sci.*, **74**, 1057–1073, https://doi.org/10.1175/JAS-D-16-0180.1.

Wildmann, N., M. Hofsäß, F. Weimer, A. Joos, and J. Bange, 2014: MASC—A small remotely piloted aircraft (RPA) for wind energy research. *Adv. Sci. Res.*, **11**, 55–61, https://doi.org/10.5194/asr-11-55-2014.

Wrenger, B., and J. Cuxart, 2017: Evening transition by a river sampled using a remotely-piloted multicopter. *Bound.-Layer Meteor.*, **165**, 535–543, https://doi.org/10.1007/s10546-017-0291-9.